CHAPTER V

OPERATIONS

The practical aspects of maintaining, balancing, and aligning the NASA-LMT are discussed along with the effects of atmospheric seeing, mirror substrate print-through, moisture condensation, and other factors directly affecting image quality.

A. Mirror Cleaning

As with a conventional glass mirror, the surface of a liquid mirror is subject to contamination from dust and debris which reduces its reflectivity. Unlike a glass mirror however, the liquid mirror Hg surface can also be torn or separated by impacts from large pieces of debris or insects. Such impacts generally result in small (1-10 cm diameter) holes in the Hg layer which yield a pitted surface and consequent reduction in reflective surface area. The mirror must therefore be cleaned periodically to return the surface to a pristine state so that the full reflectivity of Hg can be realized and a complete mirror surface restored. The frequency of cleaning varies between 1 and 6 weeks depending upon the ambient conditions. During the spring and summer months, a high pollen count and windy conditions, along with insect activity, make frequent cleaning advisable, whereas the fall and winter are more benign. Unfortunately, insect activity at NODO can become sufficiently extreme to actually halt operations. This has occurred during severe summertime infestations of migratory Miller moths.

The mirror is covered when not is use and an upper limit is set on dust concentration and wind speed to reduce contamination of the mirror surface. Using data from a particulate counter at nearby Apache Point Observatory, a limit of less than 300 particles (> 1 um diameter) is set for initiating observing. A wind speed limit of less than 25 knots is also set to prevent buffeting of the mirror and to reduce the likelihood of gypsum particles from nearby White Sands reaching the mirror. Since the formation of condensation on the mirror can also be a serious problem, observations are terminated if the ambient temperature approaches within $2\,^{0}C$ of the dew point.

Mirror cleaning is a straightforward skimming process which relies on the high density of Hg relative to the materials which contaminate the mirror. Since Hg is a dense fluid, non-metallic dust and debris particles which collect on the surface do not penetrate it, but rather float on the surface. (Metallic particles conversely can amalgamate or dissolve in Hg so special precautions are taken during machining activities near the mirror). The accumulation of dust and debris is removed by manually stopping the mirror rotation and then skimming the Hg pool (~1 m diameter) which forms in the mirror's center. The collected debris as well as the entire polyurethane mirror substrate is then wiped with a surgical cotton pad soaked with Isopropyl alcohol. The pad tends to repel Hg and attract debris, so very little Hg is removed from the mirror during this process. In fact, the Hg vacuum cleaner, which is less selective and therefore wasteful of Hg, is only used for large or tenacious contaminants and is not used to remove material collected from the pooled mirror surface. Figures V.A-1 through 6 illustrate the 1 to 2 hours duration process which is always performed with clothing and respiratory protection.

NASA-LMT: Cessation of Mirror Rotation for Hg Cleaning

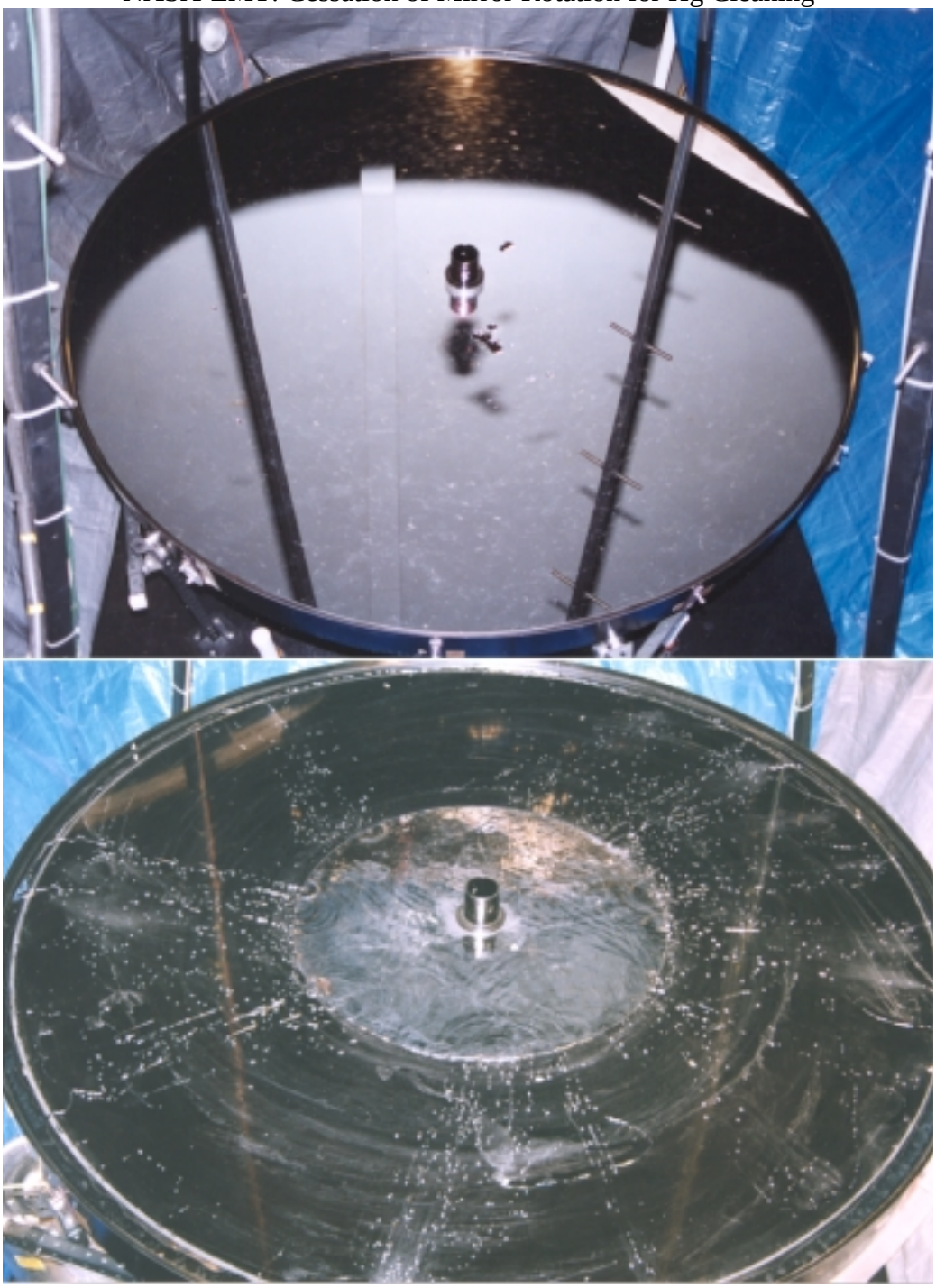

Figure V.A-1. The NASA-LMT 3.0 m primary mirror prior to and after rotation has been halted. In the upper image, the mirror is in need of cleaning after having accumulated dust and debris and having suffered insect damage (two central holes in the Hg layer). The lower image shows the stationary mirror with Hg centrally pooled and Hg streamers draining from the perimeter channel. Dirt and debris are distributed around the polyurethane substrate and floating on the Hg surface.

NASA-LMT: Dirt, Debris, and Hg Oxide on the Hg Central Pool

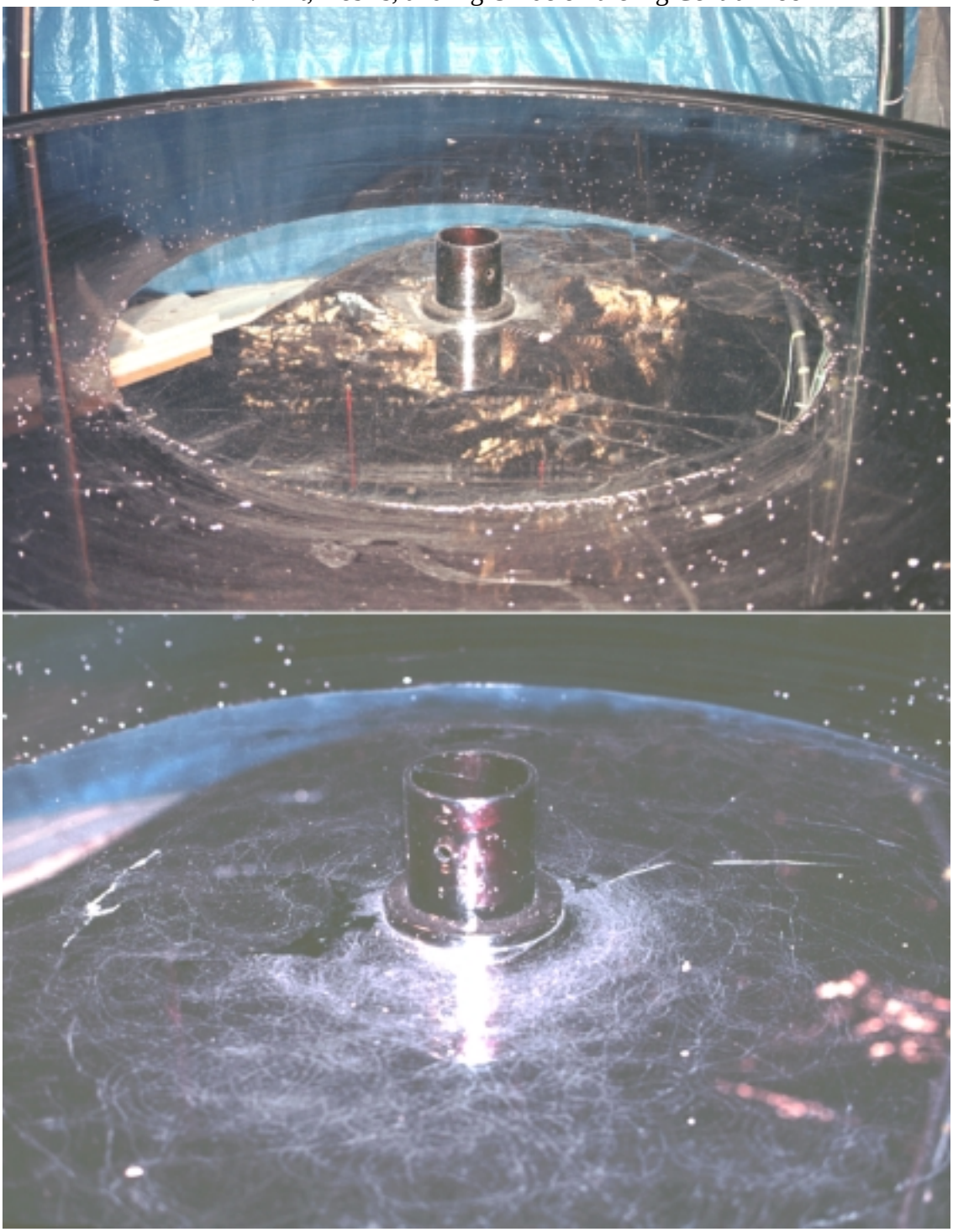

Figure V.A-2. Two views of the central Hg pool showing the consolidated layer of dirt and Hg oxide floating on the Hg surface. The oxide film appears as interlocking sheet-like patches.

NASA-LMT: Draining the Perimeter Channel

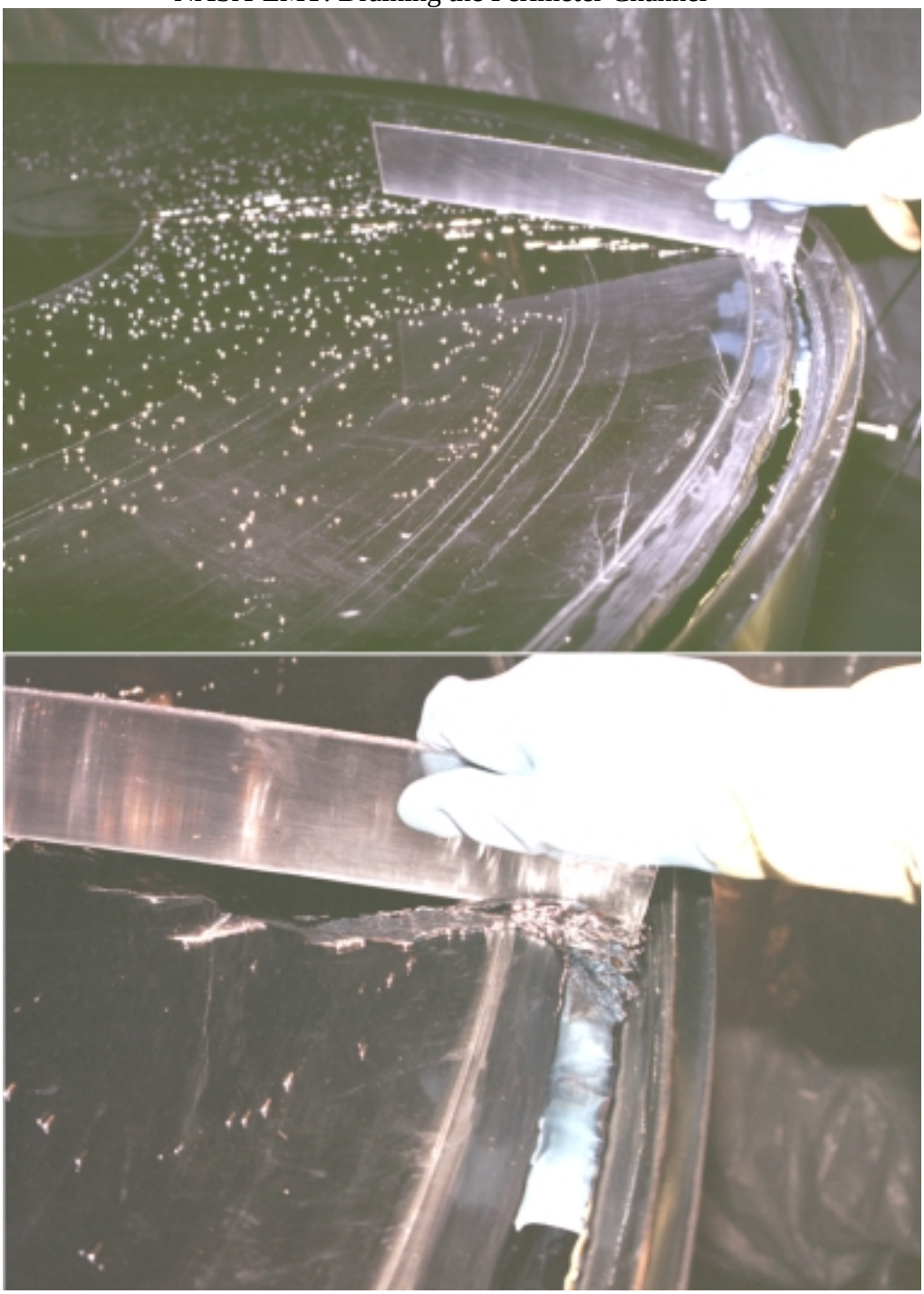

Figure V.A-3. The Hg remaining in the perimeter channel after the mirror is stopped cannot be cleared of accumulated dirt directly. The channel must be drained into the central pool by slowly rotating the mirror by hand while the plexiglass or LEXAN skimming tool is inserted in the channel. The channel can be almost completely cleared of its ~2.8 liter contents after two complete mirror rotations.

NASA-LMT: Extracting Large Debris and Clearing the Mirror Substrate of Hg Droplets

Figure V.A-4. After the perimeter channel is drained, large pieces of debris are removed from the polyurethane mirror substrate using the Hg vacuum cleaner (upper photo). (The vacuum is also used during mirror formation to extract stray pieces of debris at the sites of Hg surface tears.) Once large debris is removed, the skimming tool is used to clear the mirror substrate of all residual Hg droplets. This helps eliminate the loss of Hg when the substrate is wiped clean at the conclusion of the cleaning process.

NASA-LMT: Skimming the Central Hg Pool

Figure V.A-5. The central Hg pool is cleared of dust, debris, and oxide by using a plexiglass or LEXAN skimming tool. The tool is used to drag elements of the surface film to the mirror substrate adjacent to the pool. The tool is then laid flat against the substrate to consolidate the collected material.

NASA-LMT: Clearing the Accumulated Skimmed Material

Figure V.A-6. After consolidating the material collected from each skimming pass, a surgical cotton pad soaked with Isopropyl alcohol is used to wipe clear the accumulation. The pad attracts dirt and debris, but has minimal affinity for Hg, thus limiting Hg loss during each mirror cleaning to less than 1 milliliter. Approximately 15 passes with the skimmer are required to clean the mirror and the entire process takes 1 to 2 hours depending on the amount of accumulated dirt and debris.

B. Mirror Spin-Up

In order to be reformed, the mirror must be free of contaminants. Because the final Hg surface is generally only 1-2 mm thick, even a small piece of debris will cause the surface to tear or separate during formation and a continuous layer will not be achievable. The Hg vacuum cleaner is useful during the formation process to remove, at the site of a tear, the occasional piece of debris missed during the cleaning process. Even without particulate contamination it is very difficult to reform a mirror that has been temporarily stopped without first cleaning it, because the oxide film itself, if more than 24 to 48 hours old, will be sufficiently thick to prevent mirror formation. The oxide tends to bind portions of the Hg surface, thus preventing it from readily spreading over the mirror.

The formation process is conducted manually by spinning the mirror in such a way as to impart excess angular momentum to the Hg so that it spreads over the surface readily, and then slowing the mirror to its design angular velocity. The technique was devised by Luc Girad and replaces the laborious technique of manual spreading the Hg with Mylar sheets described briefly in Chapter I. If the mirror is clean and the Hg layer thickness is appropriate to the mirror surface deviations, at a depth no less than ~5 times the maximum vertical extent of any surface defect as determined empirically at NODO, then mirror formation can be accomplished within 2 to 5 minutes. Extremely thin (<1.4 mm) layers cannot be formed by this technique and, if required, must be generated by forming the mirror with a thicker layer and then removing Hg very slowly from the

mirror center (Borra et al. 1992). Borra has established layers as thin as 0.5 mm using this technique. Suspected print-through of mirror substrate surface defects (Section V.G-1) sets a lower limit for the NASA-LMT Hg surface thickness near the 1.61 mm presently employed.

The formation process is briefly described as follows and is illustrated in Figures V.B-1 through 4. Starting from a stationary mirror with all Hg centrally pooled and the perimeter channel empty, angular momentum is manually added to the mirror until the channel is filled and an annulus of Hg approximately 20 cm wide is formed at the mirror perimeter. This band contains about 40% of the Hg while the remainder is loosely spread around the center. The mirror at this point is spinning perhaps 30% faster than its final speed and the Hg has more angular momentum than its final state. At this point the mirror is rapidly slowed until the Hg annulus collapses to form a large central pool. All holes and gaps fill quickly and the Hg losses little angular momentum. The mirror is then rapidly brought back to a rotational velocity slightly greater than final. The Hg spreads quickly to cover the container surface, and if done properly, will completely cover the surface with perhaps only one or two small holes near the edge. At this point the mirror speed is usually slightly faster than final and it can be slowed gently by dragging ones fingers along the rim. Tenacious perimeter holes can be filled by quickly speeding or slowing the mirror and then returning it to final speed. Tears or separations at intermediate or smaller radii cannot be repaired so the mirror rotation must be stopped and the process repeated. If formation is successful, then the stabilization process begins.

NASA-LMT: Mirror Formation - Step 1

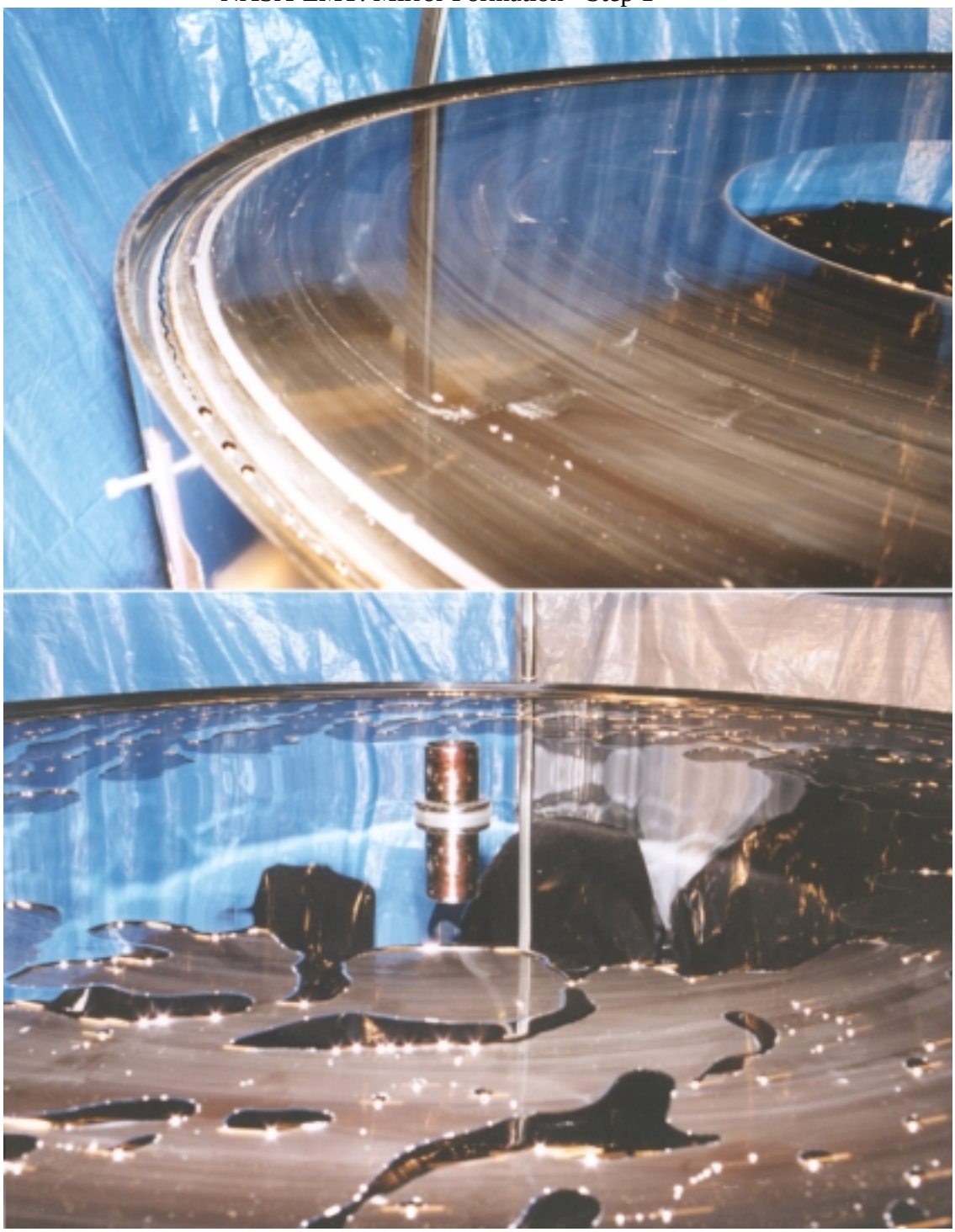

Figure V.B-1. Starting from a stationary state, the mirror is rotated manually to a speed of approximately 15 rpm (50% greater than the final design speed). This imparts angular momentum to the Hg fluid and it spreads to cover the mirror surface in small patches.

NASA-LMT: Mirror Formation - Step 2

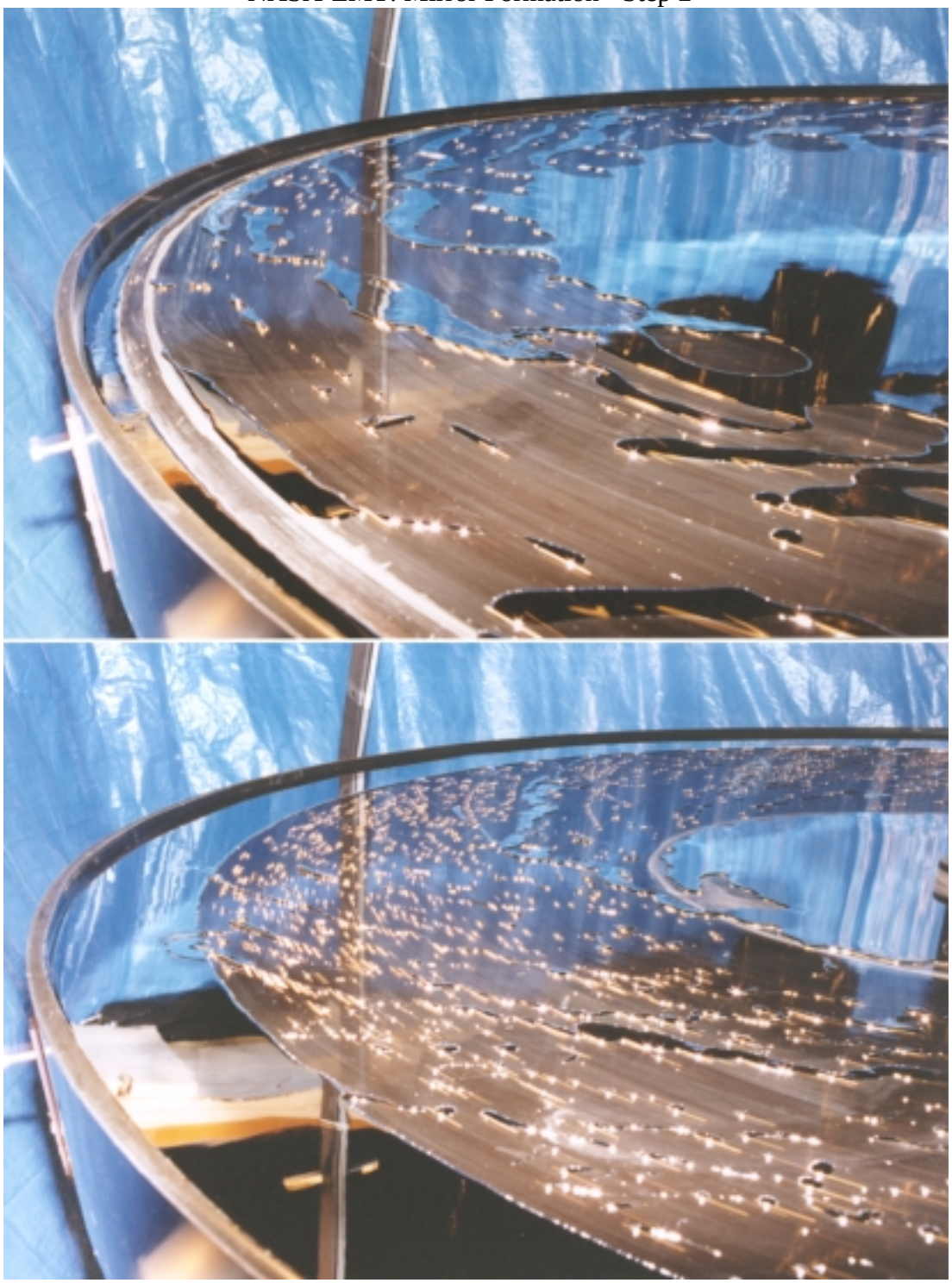

Figure V.B-2. As the mirror speed is maintained near 15 rpm, the Hg spreads to the mirror perimeter and gently fills the outer channel. The over-speed mirror rotation is allowed to continues until an approximately 20 cm wide Hg annulus forms at the mirror perimeter.

NASA-LMT: Mirror Formation - Step 3

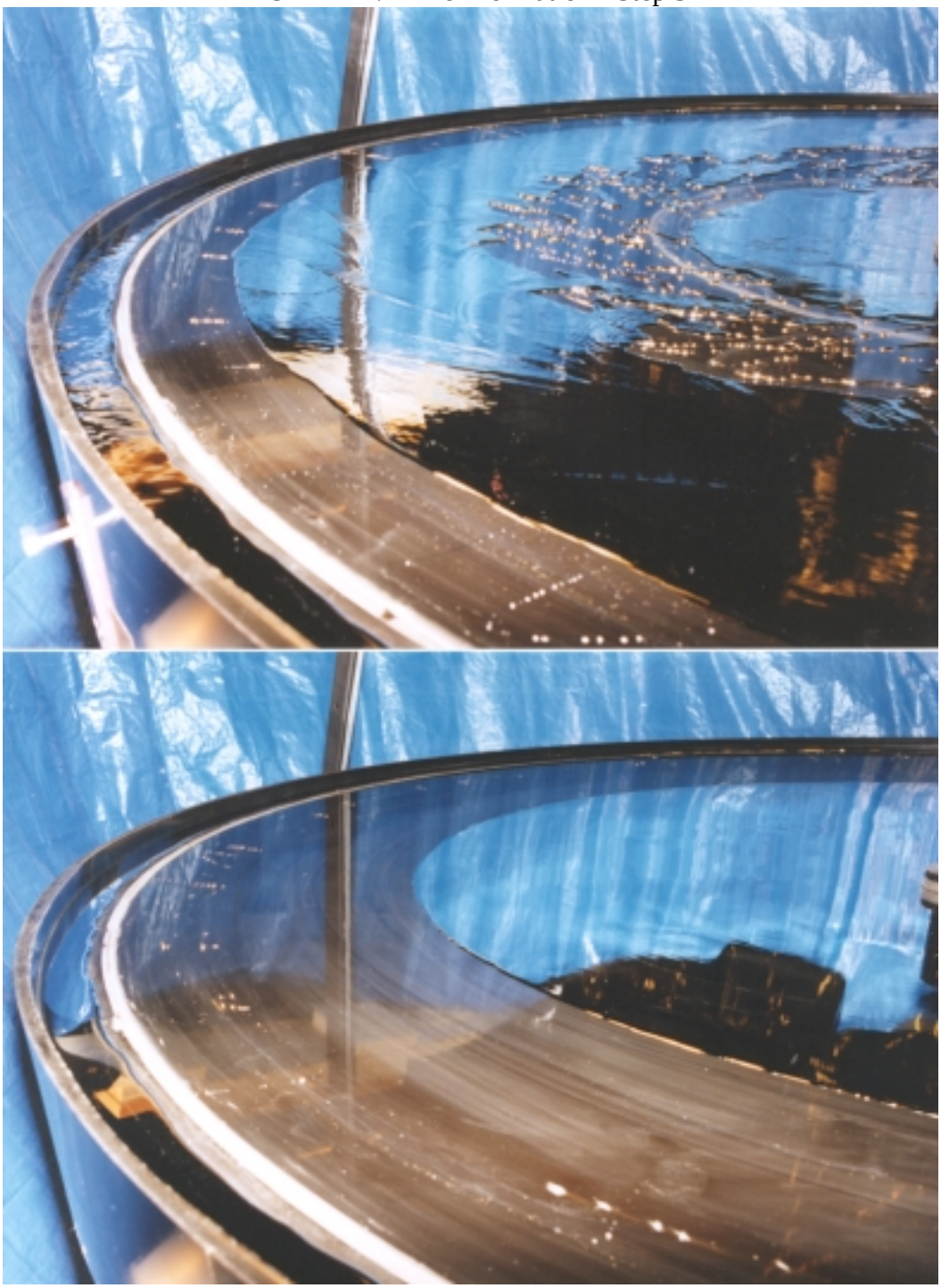

Figure V.B-3. After formation of the perimeter annulus, the mirror rotation is rapidly slowed to approximately 5 rpm (50% of the final design speed). A large continuous central pool approximately 1.5 m in diameter is quickly formed. The collapsing Hg conserves much of its angular momentum and thus the central pool is rotating faster then the mirror container.

NASA-LMT: Mirror Formation - Step 4

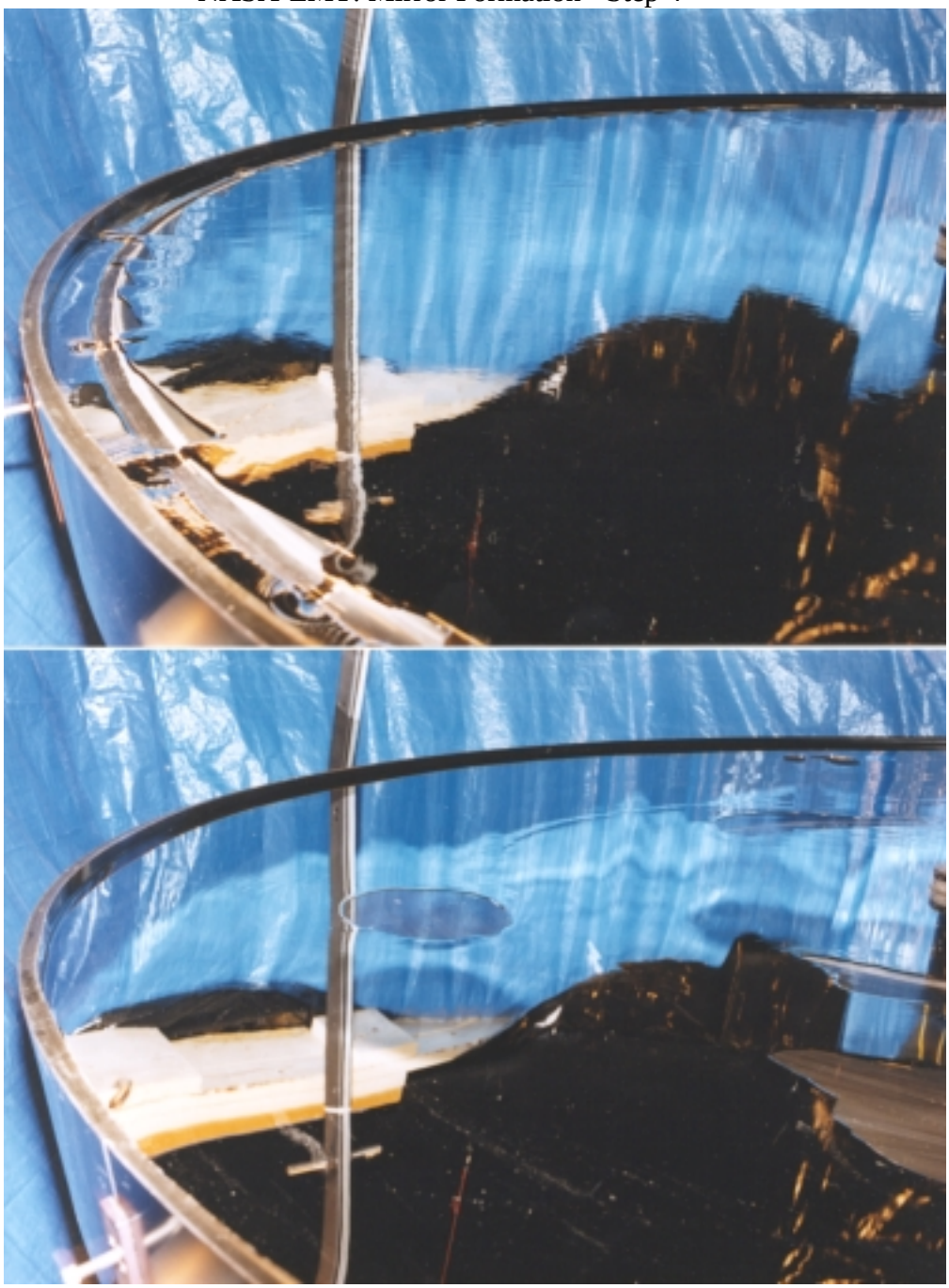

Figure V.B-4. Immediately after formation of the rapidly rotating continuous central pool, the mirror is rapidly accelerated to approximately 15 rpm. The Hg pool expands smoothly and forms a continuous sheet which connects with Hg in the perimeter channel. After the mirror is completely covered, it is quickly slowed to its approximate design speed (~ 10 rpm). In the absence of residual debris which tears the mirror surface, the mirror will stabilize in approximately 70 minutes and observing can begin thereafter. Residual debris, easily located at the site of Hg layer separation, is removed with the Hg vacuum cleaner.

C. Stabilization

Stabilization describes the process that occurs after mirror formation in which the Hg layer reaches a co-rotating equilibrium parabolic configuration. During stabilization, there is flow of Hg relative to the mirror container as angular momentum is distributed among the Hg fluid elements. The mirror must be protected from angular velocity disturbances or debris impacts during this period because separation of the fluid can occur while the Hg is flowing. If a tear does occur, the mirror rotation must be halted quickly because it is under these circumstances that large radial and azimuthal imbalances in the distribution of Hg can occur, potentially generating loads exceeding the angular load capacity of the air bearing. For this reason the mirror is monitored closely during stabilization. Approximately 70 minutes after formation, the mirror stabilizes and small angular velocity variations of less than 100 ppm will not cause the Hg layer to separate but can nonetheless degrade image quality as described in Chapter III. Similarly, debris impacts will not cause the Hg layer separation but rather will yield stable holes penetrating through Hg surface to the substrate.

The stabilization process has been described analytically using both linear and non-linear theories by Greenspan (1968). The process begins with the formation of an Ekman boundary layer at the mirror container surface within the first few revolutions following the commencement of rotation. The viscous boundary layer serves to draw in non-rotating fluid, spin it up, and then return it to the interior of the Hg layer. Fluid enters the boundary layer at smaller radii and exits at larger radii where it is then convected,

along with its added angular momentum, back to smaller radii through the interior of the Hg layer. Mass is conserved in the boundary layer, and angular momentum is conserved in the relatively inviscid interior Hg layer. Stabilization is complete when all fluid elements are in co-rotation, at which point the Ekman boundary layer dissipates Greenspan (1968). Greenspan derives the characteristic time for stabilization (t_{stab}) which is equivalent to the time required for a fluid ring to traverse the radial extent of the mirror, representing one complete circuit of fluid through the boundary layer:

$$t_{stab} = \sqrt{\frac{1}{E \cdot \Omega^2}} = \sqrt{\frac{L^2}{\nu \cdot \Omega}} \qquad \text{(V.C.a)}$$

Where:

E = Ekman number ($\nu / L^2 \Omega$; defined in Chapter III)

ν = kinematic viscosity (dynamic viscosity/density)

(kinematic viscosity of Hg is 0.0012 $cm^2/\sec$ @ 20 ^0C).

Ω = angular velocity of the system

(1.043 rad/sec for the NASA-LMT)

L = characteristic length of the system

(150 cm for the NASA-LMT)

For the NASA-LMT this yields a characteristic stabilization time of 4240 seconds or 70.67 minutes, which agrees closely with what is observed ($\pm$ 3 minutes).

The fluid transport occurring during stabilization cannot be seen by looking at the mirror surface under normal lighting conditions, but it is readily apparent under point-source illumination of the entrance pupil by stars. Figure V.C-1 shows four entrance pupil images acquired at the beginning of the stabilization process soon after the mirror was initially formed. They are MCP intensified video images with a 1/30 second exposure yielding a snapshot of the pattern exhibited by the stabilizing mercury. The distinctive quadrapole pattern, which is always observed during stabilization, does not correlate with the underlying construction of the mirror container and is therefore presumed to be attributable to the dynamics of the fluid transport. Although the detector was placed at the nominal focal point of the mirror, the examples are actually inside-focus images because the focal point of the un-stabilized mirror resides several millimeters outside the post-stabilized nominal focal point. This is attributable to the fact that the Hg is not fully co-rotating and thus the roughly parabolic mirror has a slightly longer focal length that of the stabilized mirror. As stabilization progresses, the focal point shifts toward the mirror and the entrance pupil images shrink to a proper focus. If the detector is shifted to achieve focus at the un-stabilized focal position, the image quality is extremely poor with a resolution of typically 20-30 arcseconds FWHM.

The contraction of the entrance pupil images for a detector fixed at the nominal focal position is illustrated in Figures V.C-2 through 6 and shown graphically in Figure V.C-7. The images are segments of CCD sidereal drift-scans acquired during the final 20 minutes of mirror stabilization. Beginning with mirror formation, the equivalent focal position as derived from the image diameters is approximately constant at 7.1 mm

NASA-LMT: Entrance Pupil Images Acquired During Mirror Stabilization

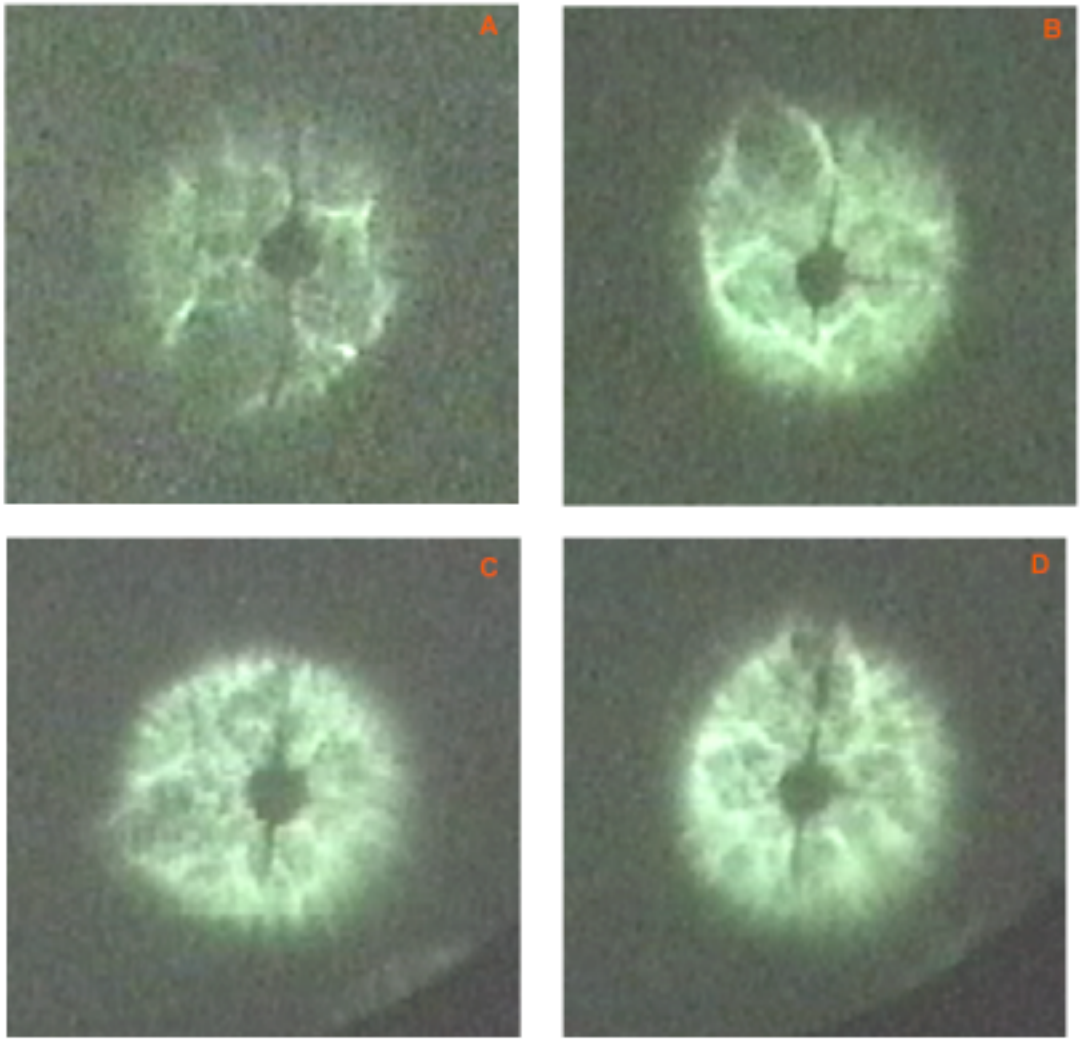

Figure V.C-1. Out-of-focus stellar images acquired a few minutes after mirror formation showing the distinctive quadrapole pattern in the entrance pupil. The pattern, which is always present immediately after mirror formation, does not correlate with the underlying mirror structure and is therefore presumed to be related to the characteristic dynamics of fluid and angular momentum transport during stabilization. The shadow of the prime focus assembly and its support structure is visible. These images were acquired with the MCP intensified video camera and a 1/30th second exposure time. Rotation: CW

NASA-LMT: Mirror Stabilization I

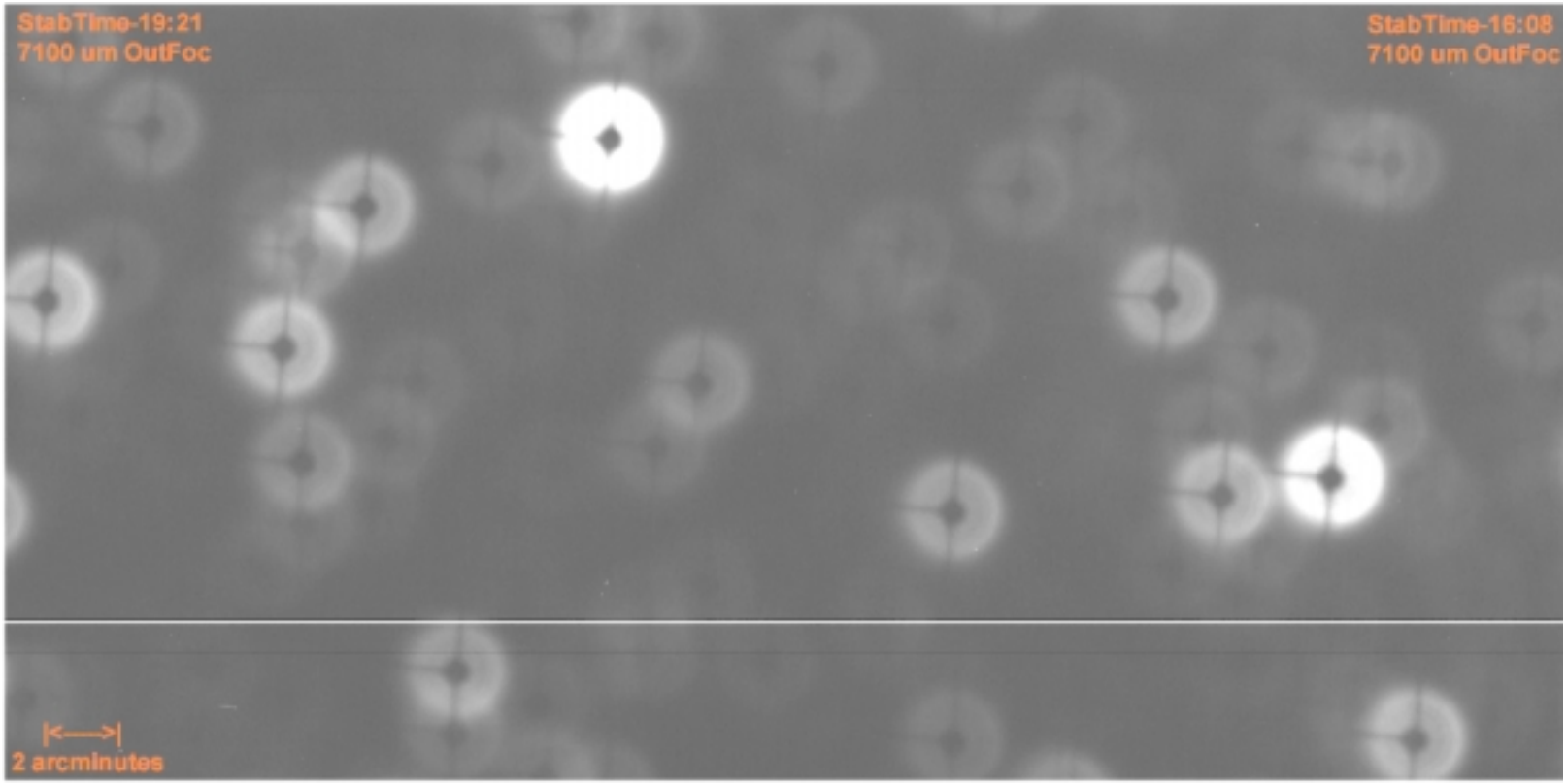

Figure V.C-2. Stabilization sequence illustrating the process of mirror stabilization after mirror formation. Immediately after mirror formation the mercury is not co-rotating or distributed in parabolic form over the mirror container. The mirror focal point resides 7.1 millimeters outside of the post-stabilization position and image quality is very poor at this shifted focal point. After approximately one hour, the mercury co-rotates, forms a parabolic surface, and the focal point rapidly moves to the nominal focal position. The TDI image above was acquired at the nominal focus approximately 50 minutes (50:00) after mirror formation and 19:21 prior to stabilization. The image ends 03:13 later, 16:08 prior to stabilization, with no change in equivalent focal position as determined by image size. The subsequent four images form a continuous strip showing the rapid transition to a stablized mirror. The horizontal white line is an artifact of the LSP 2K CCD used to acquire this data.

NASA-LMT: Mirror Stabilization II

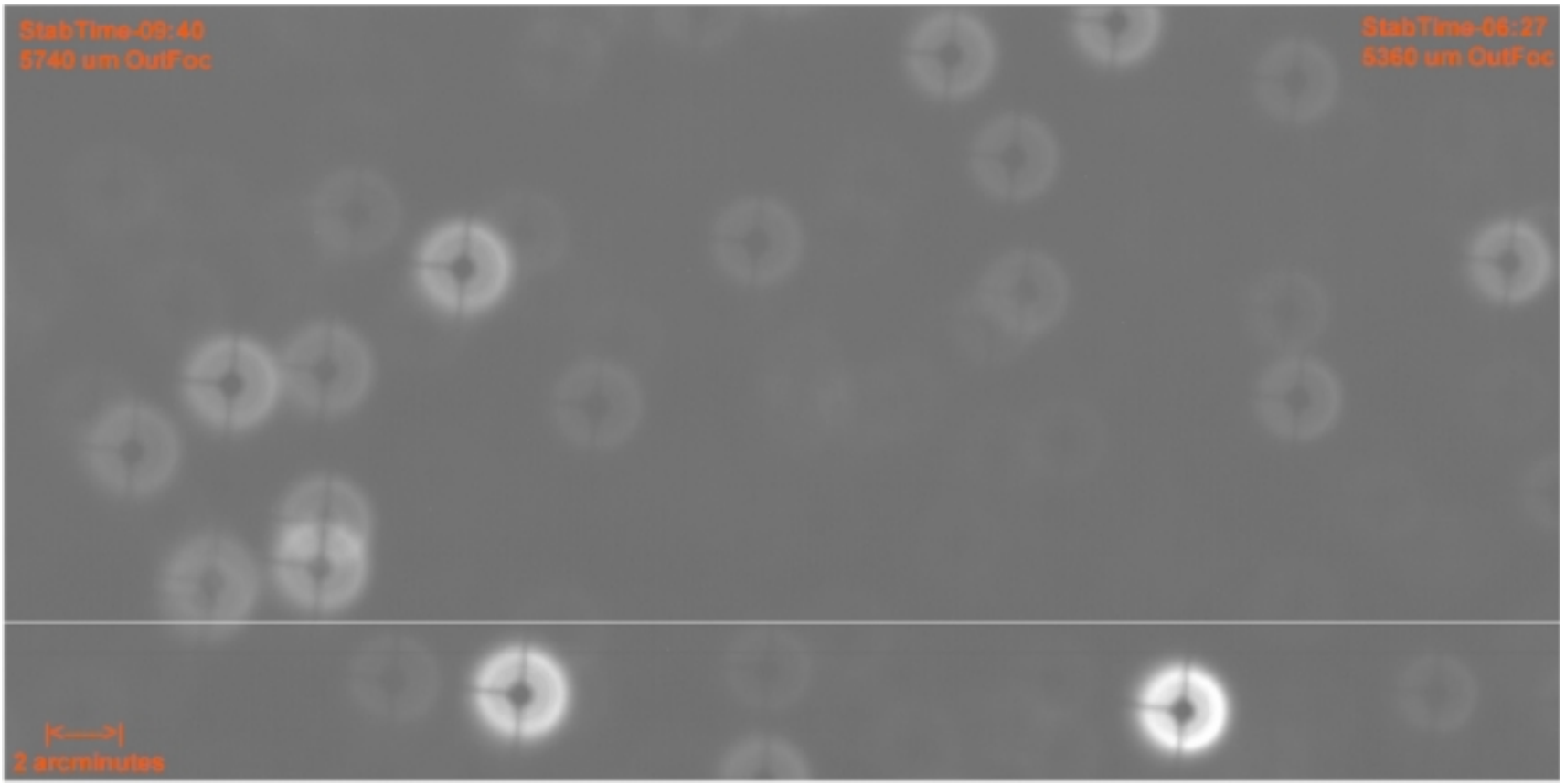

Figure V.C-3. Stabilization sequence illustrating the process of mirror stabilization after mirror formation. The TDI image above was acquired at the nominal focus starting at a time 09:40 prior to stabilization. At the beginning of this frame, the focus has shifted -1360 um (towards the mirror) from the previous image (as determined by size of the first complete stellar image). The frame ends 03:13 later, 06:27 prior to stabilization, with a change in equivalent focal position of -380 um. The mirror is rapidly stabilizing.

NASA-LMT: Mirror Stabilization III

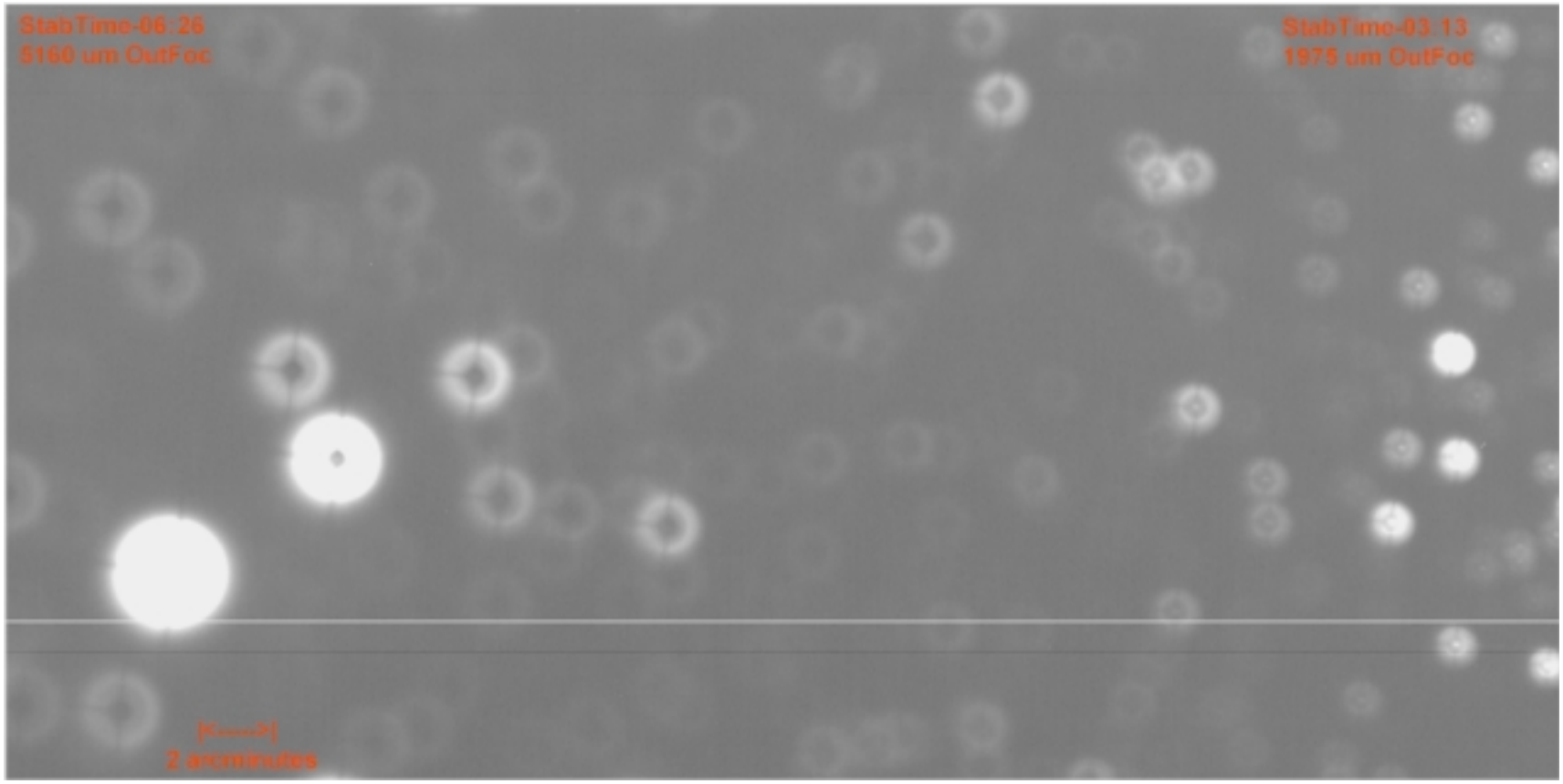

Figure V.C-4. Stabilization sequence illustrating the process of mirror stabilization after mirror formation. The TDI image above was acquired at the nominal focus starting at a time 06:26 prior to stabilization. At the beginning of this frame, the focus has shifted -200um (towards the mirror) from the end of the previous image (as determined by size of the first complete stellar image). The frame ends 03:14 later, 03:13 prior to stabilization, with a change in equivalent focal position of -3185 um. Stabilization continues rapidly.

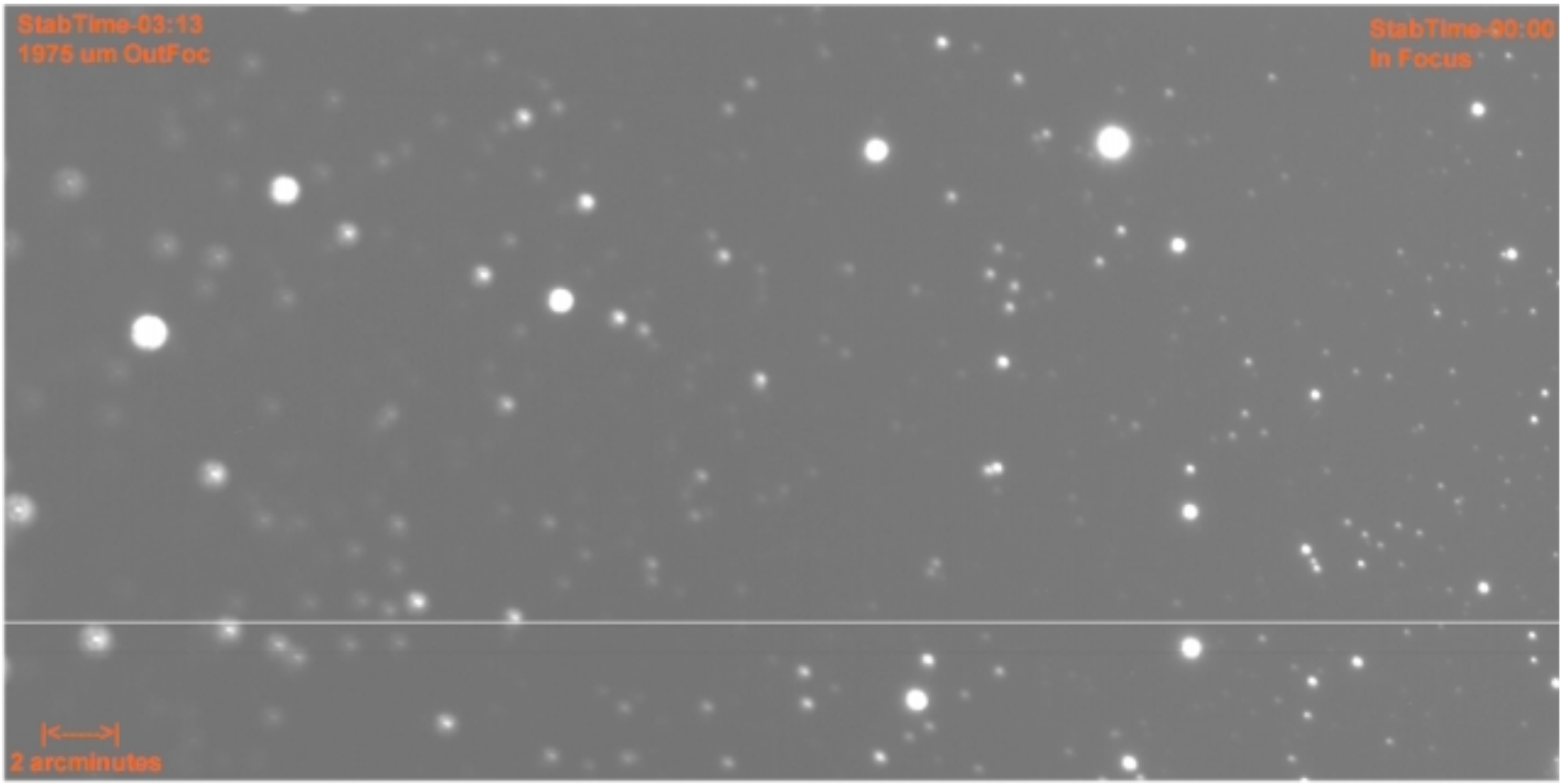

Figure V.C-5. Stabilization sequence illustrating the process of mirror stabilization after mirror formation. The TDI image above was acquired at the nominal focus starting at a time 03:13 prior to stabilization. The beginning of this frame has measured stellar images essentially continuous with the previous frame. The frame ends 03:13 later, at stabilization, with a change in equivalent focal position of -1975 um. Stabilization is complete and images are in focus.

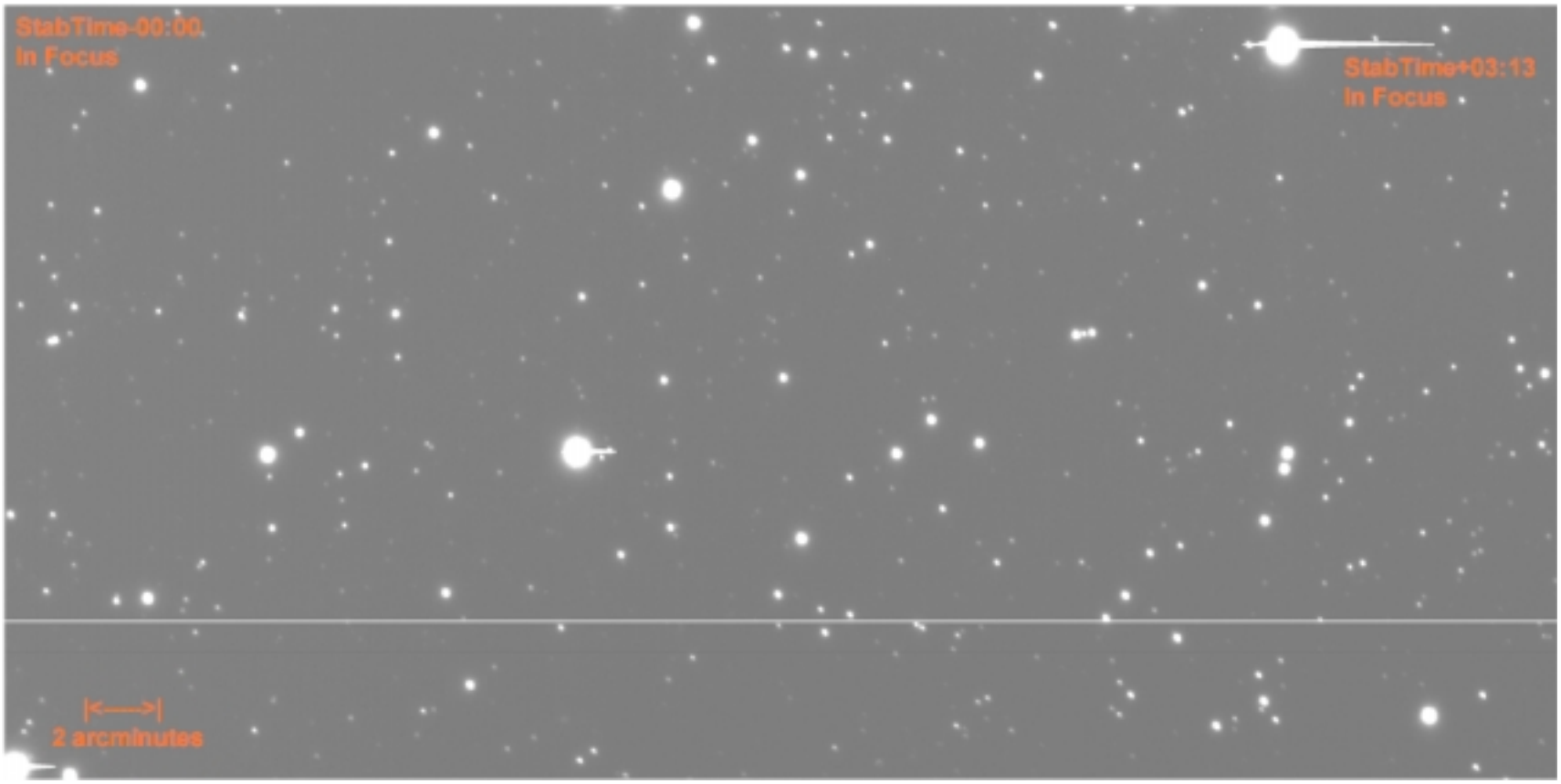

Figure V.C-6. Stabilization sequence illustrating the process of mirror stabilization after mirror formation. The TDI image above was acquired at the nominal focus starting at the time the mirror had stabilized. At the beginning of this frame, the focus has remained constant relative to the end of the previous image (as determined by size of the first complete stellar image). The frame ends 03:13 later, with no change in equivalent focal position. Mirror stabilization is complete and image focus is stable.

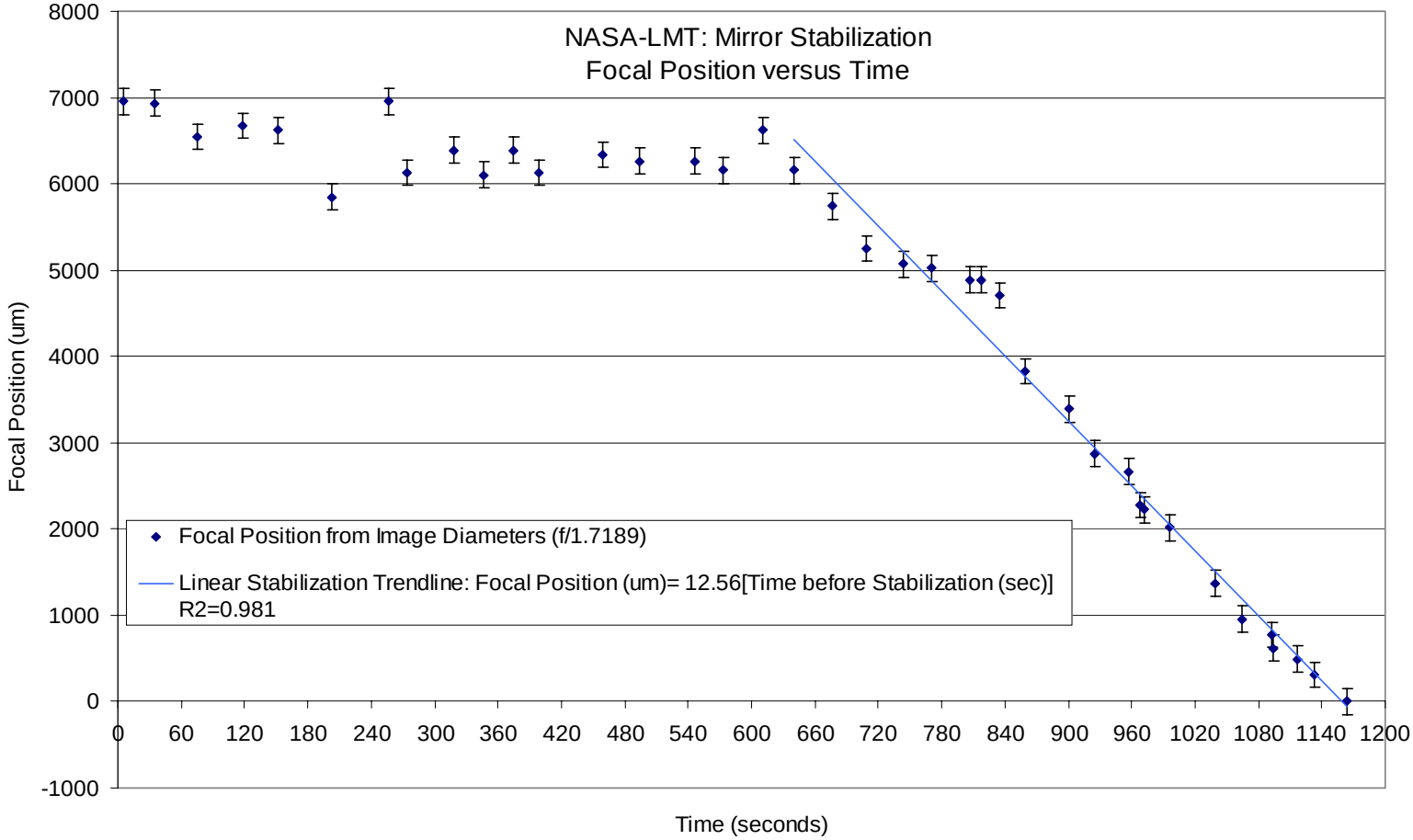

Figure V.C-7. Focal position derived from image diameter as a function of time during mirror stabilization. The data, beginning 50 minutes after mirror formation, indicates an approximately constant focal position of 6 to 7 mm outside focus. At 60.7 minutes after mirror formation, however, the image diameters shrink and the focal position rapidly moves to its nominal position (0) in approximately 8.7 minutes. The rapid portion of the stabilization phase has a slope of 12.56 um/sec as indicated by the blue line. Error bars are +-150um (+-10 pixels).

outside nominal focus. At roughly16 minutes prior to stabilization, the focus begins to drift to 6mm outside nominal focus position where it remains until approximately 8.7 minutes prior to stabilization. A transition then occurs and the focal point rapidly moves to the stable nominal focal position at a rate of 12.56 um/sec. At this point, ~ 71 minutes after formation, the mirror has stabilized and image quality is nominal.

D. Mirror Tilt

As described in Chapter III, it is essential that the rotational axis of the mirror be as closely aligned with the gravitational vector as possible, preferably parallelism within 0.1 arcsecond should maintained (Table III.D-1). The mirror should be re-leveled after every cleaning, as thermal fluctuations can cause minute shifting (~0.3 arcsecond) of the I-Beam and its supporting screws and pads. A spirit level attached beneath the mirror at its hub as shown in Figure V.D-1, is used to determine level. The operation is performed iteratively, by first leveling one base of the I-Beam triangle and then the altitude or bisector of this chosen base. Absolute level is determined by performing180 degree rotations of the spirit level (by rotating the mirror) with it first parallel to the base and then anti-parallel. The adjusting screws at opposite ends of the chosen base are moved gently until, upon 180 degree rotation, the level's bubble does not move. Once a base is leveled, the same operation is performed on the bisector. Now, if the mirror is rotated to any arbitrary position, the bubble should retain a fixed position in the site glass. With care, the 5 arcsecond/division spirit level can be read to approximately ± 0.2 arcseconds.

NASA-LMT: Primary Mirror Undercarriage

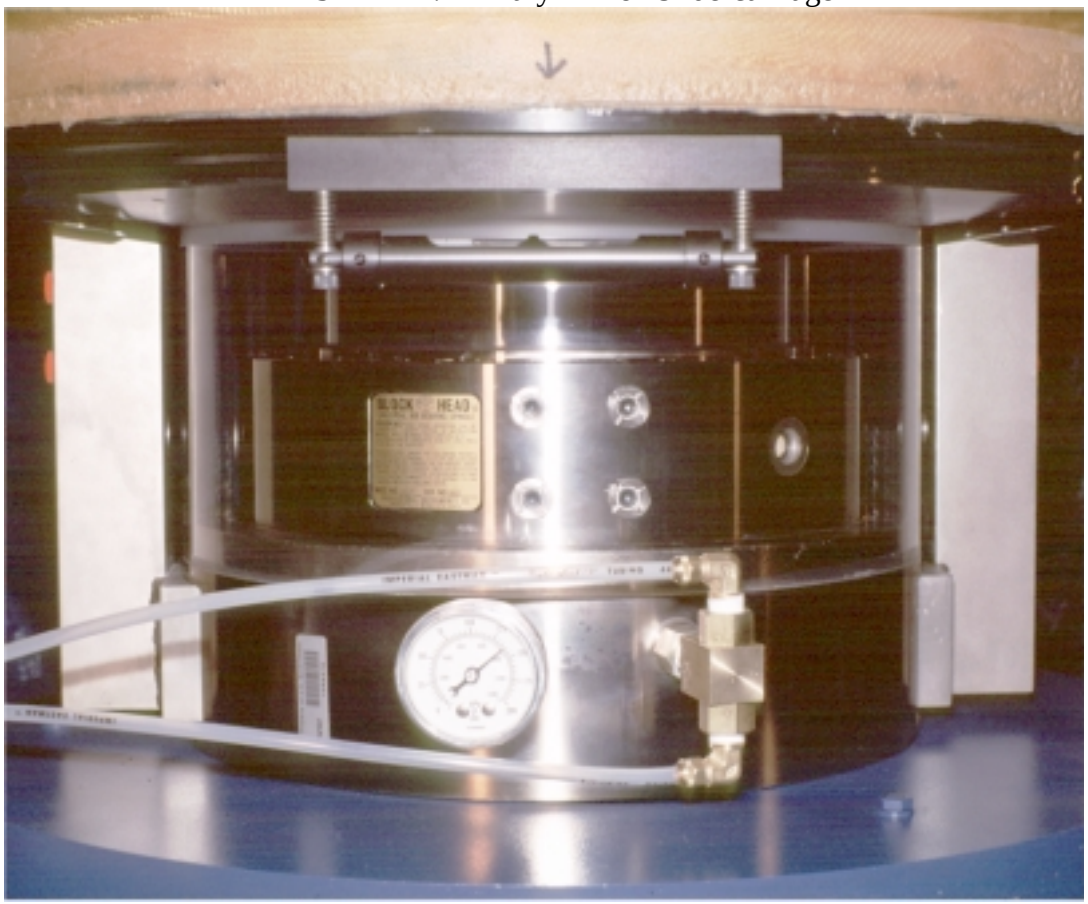

Figure V.D-1. View of the undercarriage of the NASA-LMT showing the spirit level attached to the lower hub of the mirror container. The level is used to align the rotational axis of the mirror with the local gravity vector. If upon mirror rotation, the spirit bubble does not move, the mirror is level. The level can be read carefully to +-0.2 arcseconds. The Professional Instruments 10R air bearing, air lines, and pressure gauge are also visible.

An electronic level is available which allows parallelism to be determined even more accurately to ± 0.04 arcsecond.

Figure V.D-2 shows the results of an experiment conducted to characterize the image degradation associated with mirror tilt, but unfortunately the atmospheric seeing was poor (~3 to 4 arscecond FWHM) during the test. These images were made by intentionally tilting the mirror while in rotation, using the electronic level as a relative reference. The contour and surface plots do not help to significantly differentiate the three trials. The only discernable difference is the appearance of an enhanced annular donut shaped ring in the image acquired with 7.0 arcseconds of mirror tilt relative to the gravitational vector. This may be a real effect, but the tests will need to be repeated under better seeing conditions to be useful.

E. Mirror Dynamic Balance

Although the mirror's surface after stabilization is parabolic, the Hg layer thickness is not uniform because the mirror substrate has localized low and high regions that deviate from a true parabola. This slight variation in Hg layer thickness yields an imbalance in weight distribution which displaces the mirror's center of mass from the rotational axis. Because the mirror subsystem has finite angular stiffness, its response to this imbalance can be separated into two components: a global tilting of the mirror container and a coning or wobbling motion of the rotational axis. These two components are manifest as a cycloidal motion of star images in the trails produced by drift-scans at a

NASA-LMT: Mirror Tilt Demonstration

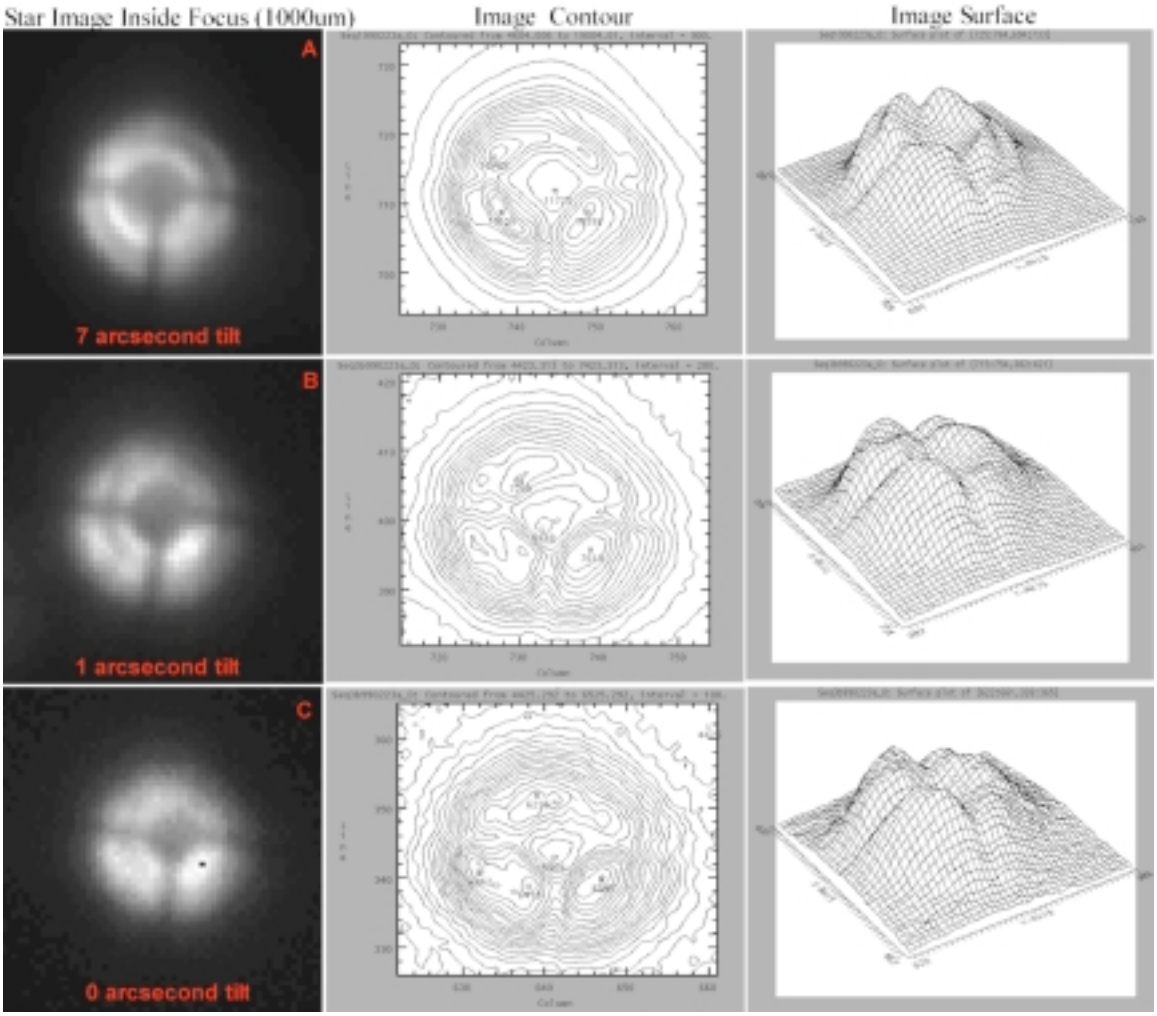

Figure V.D-2. Three entrance pupil images are presented for rotational axis misalignments (tilt) of 7, 1, and 0 arcseconds respectively. Contour and surface plots are also provided to help differentiate the images and reveal any distinguishing features. A bright circular annulus at approximately 50% of the mirror radius appears to become more prominent as the mirror tilt increases, but this result is inconclusive due to the poor seeing conditions (~3 to 4 arcseconds FWHM) while this data was acquired.

non-sidereal rate.

For the case of the coning rotational axis, the cycloidal motion arises from the entire parabola executing a wobbling motion which produces images tracing circular paths which are then overlaid on a detector that is drift-scanning in one direction. The convolution of the detector and the parabola motion yields stellar images which alternately move with, orthogonal too, and against the detector scan. This cycloidal motion, which is always present if the mirror is not dynamically balanced, degrades the image quality and therefore must be removed. By the judicious placement of weights at different azimuthal positions at the mirror's perimeter, the Hg layer can be redistributed and the mirror's center of mass realigned with the rotational axis. Weight placement is performed iteratively by repeatedly inspecting trailed images to minimize the orthogonal excursions. In addition to the cycloidal motion, there is further image degradation arising from the inability of the Hg layer to form a truly parabolic shape due to the wobbling rotational axis. Proper dynamic balance is thus critical.

For the case of the tilted mirror container, there is no discernable effect in the steady state because the Hg layer compensates, still forming a parabolic surface regardless of the global tilt of the container. The container tilt can be observed however as a transient response to an induced imbalance. Since the Hg layer cannot adjust instantly to a global tilt of the container, the entire parabolic surface tilts for a few minutes after the intentional introduction of an unbalanced load. This gives rise to a transient cycloidal motion similar to that of the rotational axis coning, but of much larger amplitude. This motion dissipates after the Hg re-establishes a parabolic surface.

The amplitude of the cycloids attributable to each mode of tilt is determined by the angular torque exerted by the unbalanced mirror and the angular stiffness of the subsystem components. The coning of the rotational axis depends on the angular stiffness of the components that support it: the I-Beam base with its bolted interface to the air bearing via the air bearing carriage, and the intrinsic stiffness of the air bearing itself. Similarly, the air bearing-mirror coupling and mirror stiffness determine the global tilt of the mirror container with respect to the rotational axis. From Chapter IV, the I-Beam base compliance and air bearing compliance are known, but the compliance of the air bearing to I-Beam base interface was not measured separately. It is a component of the measured stiffness of the entire air bearing assembly and is reasonably assumed to be no more than ¼ of the assembly compliance which remains after subtracting the component attributable to the air bearing itself. This assumption is based on the nature of the lapped 12-bolt interface between the I-Beam base and air bearing carriage and the likely flexure in the conical hub which interfaces the air bearing to the bottom of the mirror container. This latter interface possesses the remaining ¾ of the compliance. The I-Beam base, air bearing and air bearing to I-Beam interface moment stiffness values of $2.60x10^6\ N \cdot m$/rad, $13.60x10^6\ N \cdot m$/rad, and $21.17x10^6\ N \cdot m$/rad, respectively, thus imply an orthogonal peak-to-valley (P-V) amplitude to the stellar trail cycloids, for an applied torque, of 0.10 arcseconds/N-m. The mirror container and air bearing to mirror interface stiffness values of $1.78x10^6\ N \cdot m$/rad and $7.06x10^6\ N \cdot m$/rad, respectively, imply an orthogonal P-V amplitude, in response to an angular load, of 0.145 arcseconds/N-m.

Figure V.E-1 demonstrates the transient behavior of global tilt on trailed stellar images after the placement of an unbalancing load at the perimeter of the previously stabilized and dynamically balanced NASA liquid mirror. In this example, the 3.3 kg lead weight exerts a torque on the mirror subsystem of 48.6 N-m causing a global tilt of 7.05 arcseconds which agrees well with the P-V amplitude of 8.6 arcseconds obtained by extrapolating backwards to the time of weight placement based upon the measured P-V decay of the stellar cycloids of 1.25 arcsecond/minute.

The final trail in Figure V.E-1 shows the steady state cycloidic motion revealing the effects of the remaining coning error after the transient behavior has dissipated and the Hg layer has compensated for the global mirror tilt. The predicted steady state coning error P-V amplitude based upon the I-Beam base compliance described above is 4.86 arcseconds, but the actual measured P-V amplitude is only approximately 0.6 arcsecond (1 pixel). Since the angular moment stiffness of the I-Beam base is fairly accurately determined (Chapter IV), and the resultant angular load after the Hg has flowed to reform the parabolic surface is at least as great as the originally applied load, an alternate explanation is proposed. The bulk of the discrepancy is possibly due to the inability of the I-Beam subsystem to respond instantaneously to the rotating mirror imbalance. Angular moment stiffness measurements are made with stationary system components allowing ample time to respond to the applied load. The dynamic load resulting from the unbalanced rotating mirror may not allow sufficient time for the full deflection to occur at any given azimuthal position. Measurements made with the electronic level sensor located at the I-Beam base with a rotating unbalanced mirror confirm the P-V amplitude

Mirror Dynamic Balance – Transient Response

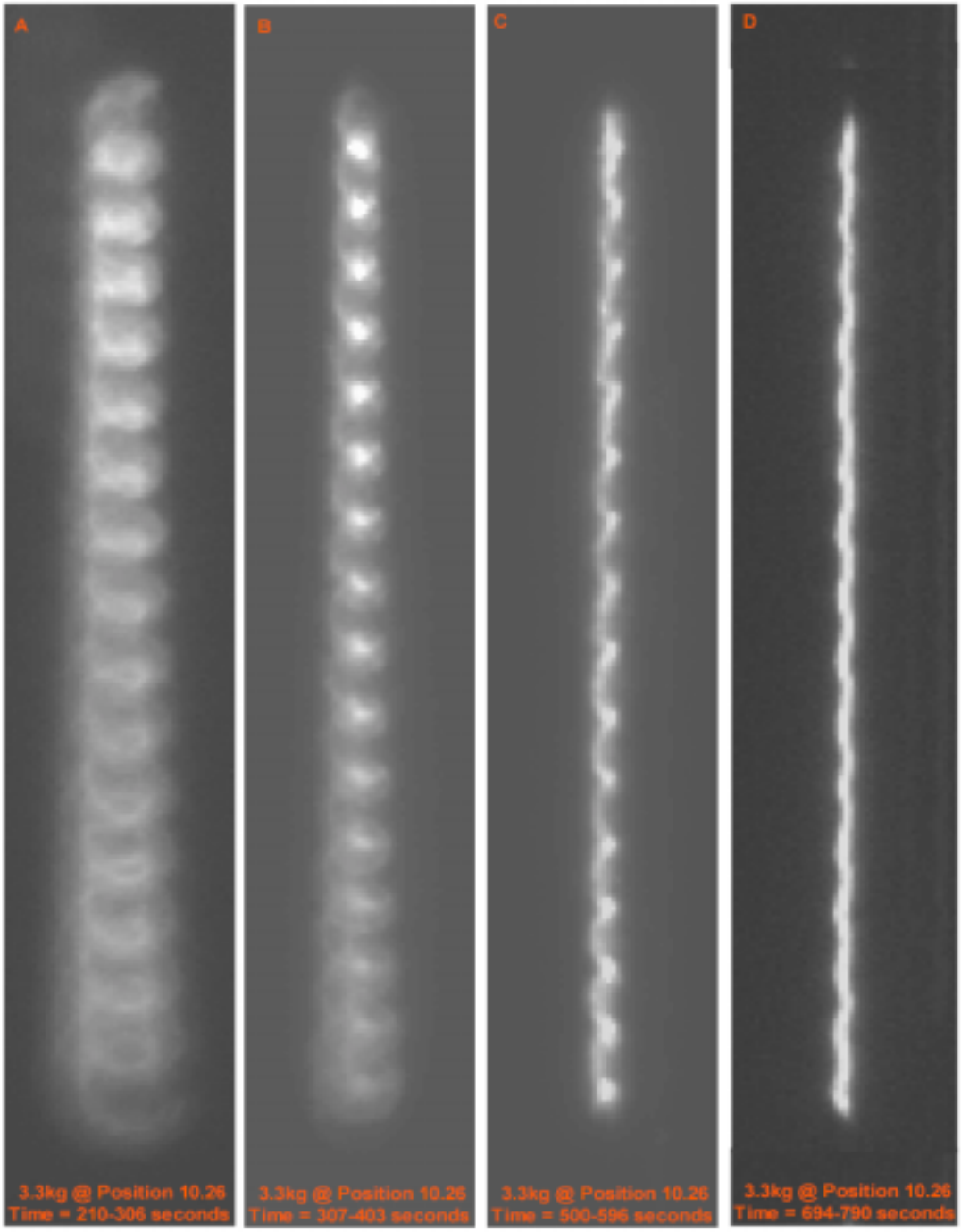

Figure V.E-1. An illustration of the transient response of the NASA liquid mirror to the application of a 3.3 kg load (48.6 N-m) at the mirror perimeter. The cycloidic motion is due to convolution of the rotating tilted parabola and the unidirectional CCD drift-scan. Each strip is 28.8 arcseconds wide (48 pixels) and each stellar trail represents 16 mirror rotational periods or 97 seconds of time. The P-V amplitude decay rate is 1.25 arcseconds/minute and results from the redistribution of Hg to compensate for the induced tilting of the mirror container. The initial P-V amplitude agrees with the angular moment stiffness prediction.

seen in the stellar trails. Since the static angular moment stiffness measurements yield a value almost an order of magnitude more compliant than the value implied by the stellar trails and the electronic level measurements, it is reasonable to assume that the different response time explains the discrepancy. The discrepancy is fortuitous as it greatly dampens the effect of mirror imbalance making it easier to compensate with the application of perimeter weights.

Figures V.E-2 through 4 illustrate the steady-state cycloidic motion resulting from coning error for various angular loads induced at the perimeter of a fully stabilized and initially dynamically balanced liquid mirror. The orthogonal excursions in the balanced reference image of Figure V.E-2 are primarily due to atmospheric seeing rather than mirror imbalance. From the figures it is apparent that even a modest load of 0.91 kg at the mirror perimeter (13.4 N-m) must be corrected. The NASA liquid mirror is currently dynamically balanced with a compensating load of 3.63 kg placed at the 5^{th} (of 12) azimuthal position. Figures V.E-5 and 6 show the variation in light intensity along the trajectory of a star trail once again emphasizing the need for proper dynamic balance in order to prevent degradation of the image PSFs.

F. Prime Focus Alignment

The prime focus assembly must be aligned so that the optical axis of the corrector and the CCD coincide with the optical axis of the primary mirror. This is achieved iteratively by comparing out of focus images and making lateral or tilt adjustments to the PF assembly. The method is extremely sensitive to lateral displacements but is relatively

Mirror Dynamic Balance I

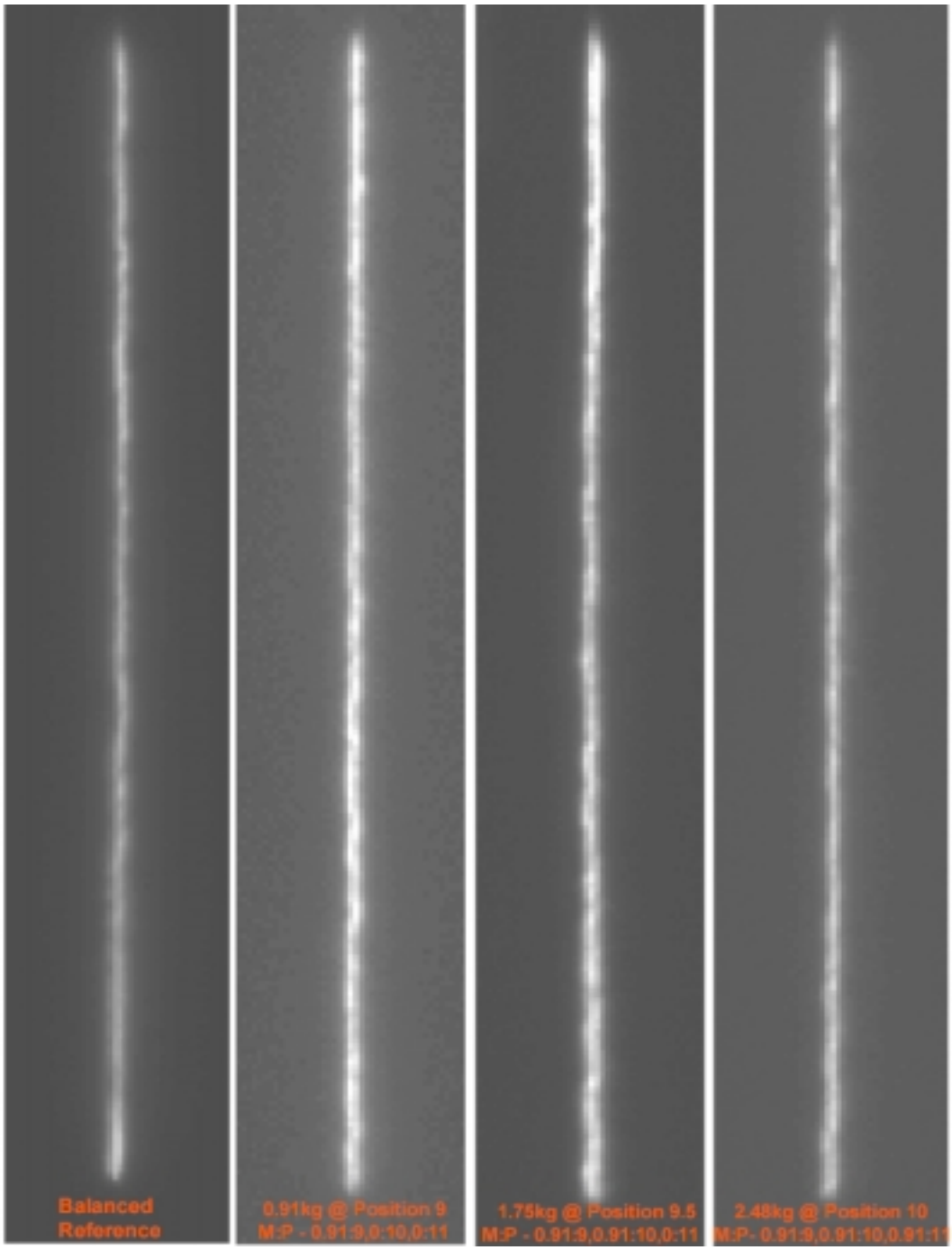

Figure V.E-2. Mirror Dynamic Balance Sequence illustrating the effect of dynamic mirror imbalance on trailed stellar images. Reference image is for a dynamically balanced mirror achieved via the judicious placement of rim weights. Subsequent images demonstrate increasing imbalance. The 97 sec TDI exposure is equivalent to 16 mirror rotational periods. The oscillating signature resulting from mirror wobble is increasingly visible as the imbalance increases. This oscillation can broaden the PSF by several arcseconds - significantly reducing optical resolution.

Mirror Dynamic Balance II

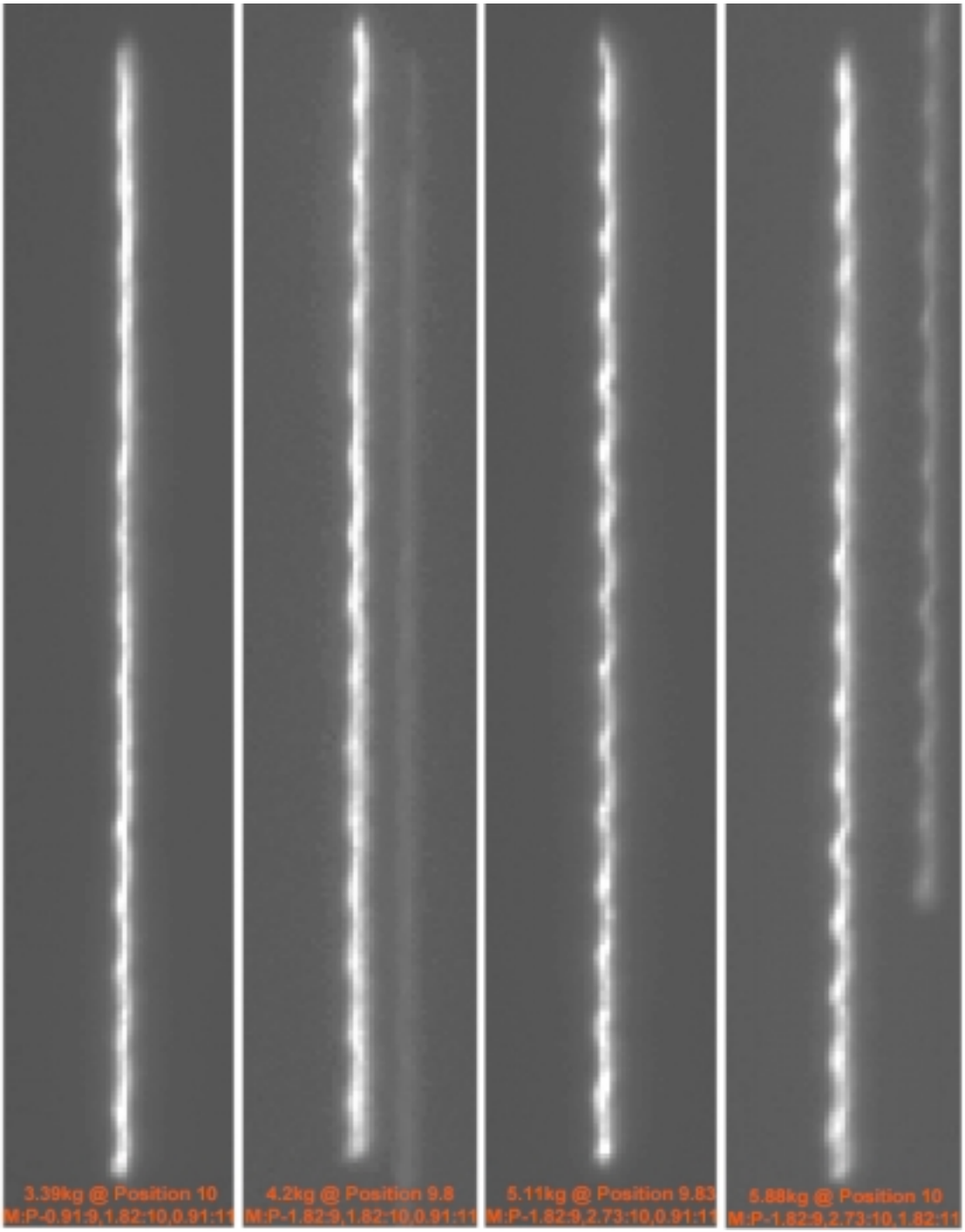

Figure V.E-3. Mirror Dynamic Balance Sequence continued. The dynamic imbalance is increasing from left to right via the intentional application of more weight at the mirror perimeter. The sixteen mirror rotational periods are distinctly evident in these 97 second duration TDI trailed stellar images. Note the cycloidic motion due to the wobbling image tracking alternately with and against the CCD drift scan direction during each rotation of the mirror.

Mirror Dynamic Balance III

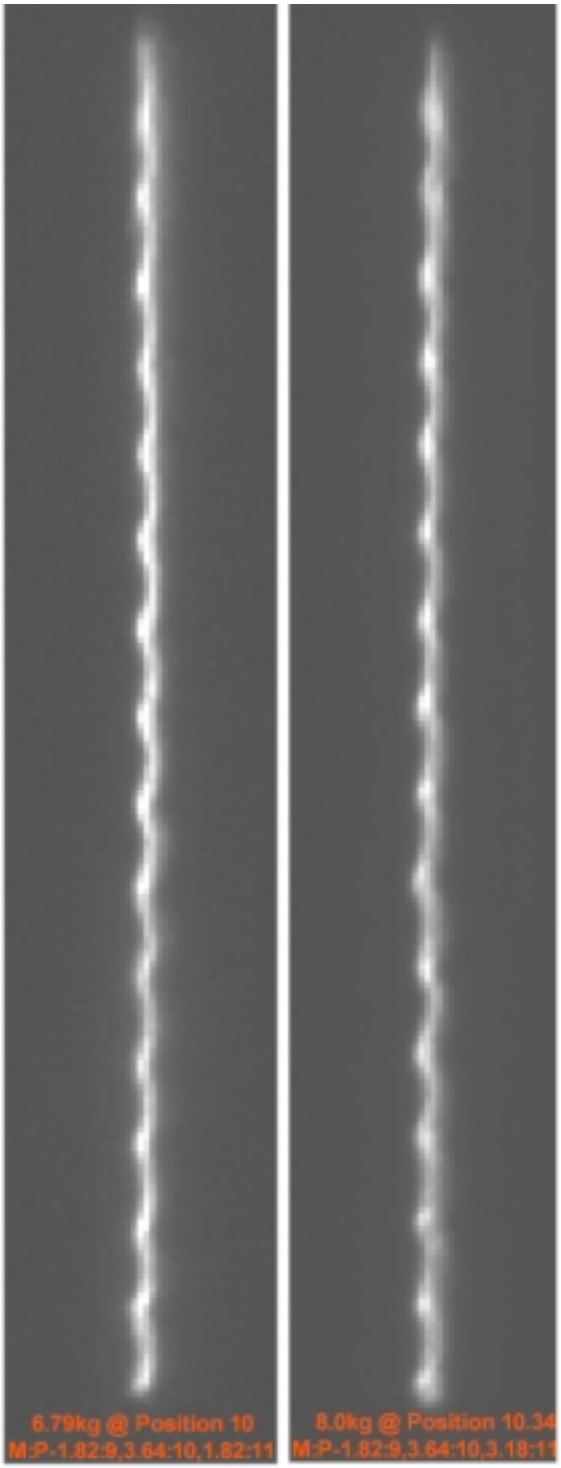

Figure V.E-4. Mirror Dynamic Balance Sequence continued. These images result from a significant dynamic imbalance. The sixteen mirror rotational periods are distinctly evident in these 97 second duration TDI trailed stellar images. The cycloidic motion due to convolution of the wobbling image and the CCD drift scan is also easily visible.

Mirror Dynamic Balance - Balanced Mirror with Weights Applied

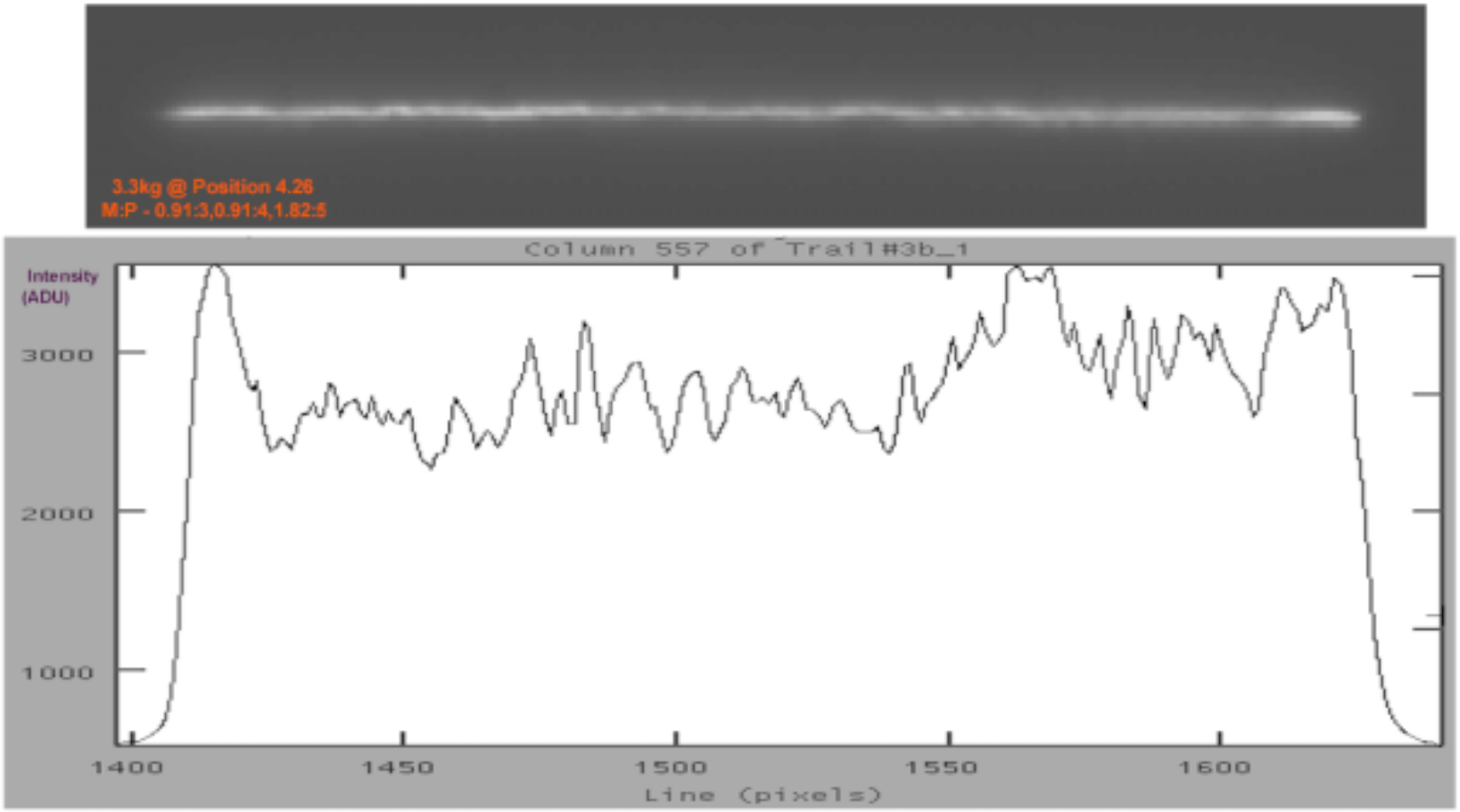

Figure V.E-5. An intensity profile (lower frame) passing along the central row of the trailed stellar image (upper). The intensity profile is dominated by seeing effects and shows only weak evidence of the mirror rotational period. As indicated, the equivalent mass and perimeter position are 3.3 kg and 4.26 respectively. The residual lateral variations in image intensity are primarily due to atmospheric seeing.

. Mirror Dynamic Balance - Intrinsic Imbalance with No Balance Weights Applied

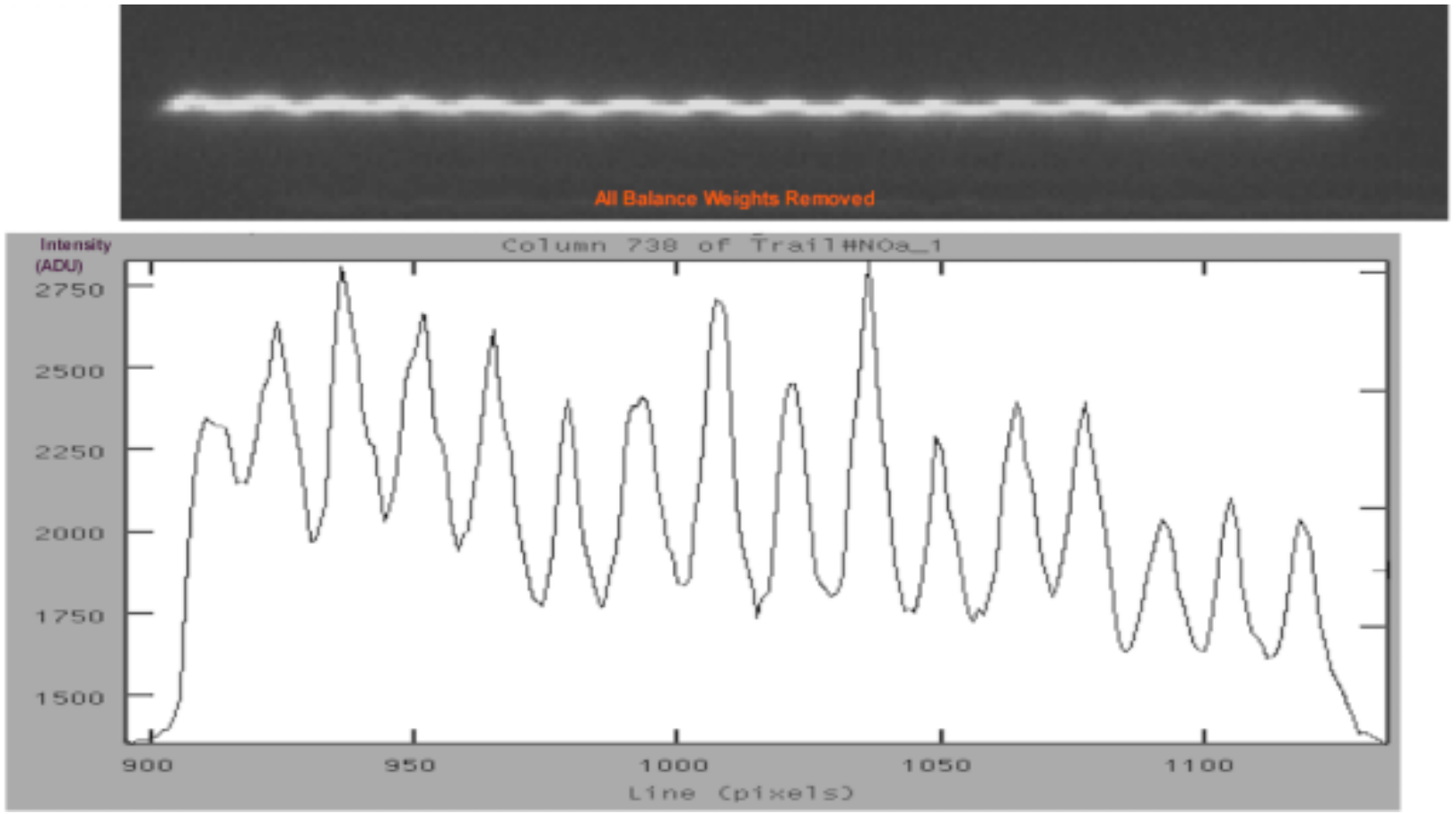

Figure V.E-6. An intensity profile (lower frame) passing along the central row of the trailed stellar image (upper). The intensity profile is dominated by mirror wobble while seeing effects are masked. The oscillations correlate with the rotation period of the mirror - 16 oscillations in this 97 second drift scan exposure. This is the intrinsic imbalance of the mirror in the absence of any balance weights.

insensitive to tilt adjustments. Figures V.F-1 through 4 show the effect of lateral displacement on the out-of-focus images and the resulting stellar images generated with both a properly aligned and misaligned PF assembly. Using this technique, lateral alignment to +-50 um can be achieved. An alternative method using a pair of vertically aligned lasers was found useful for rough alignment during initial installation of the PF assembly, but because of the lack of image quality feedback, it is not sufficiently accurate for precision lateral positioning. The laser beams are directed at the mirror with the reflected beams crossing at the axial focal point giving a reference for gross alignment.

Figure V.F-5 illustrates the effect of PF tilt on a trailed stellar image. In this example the tilt error is in the East-West direction and is thus aligned with the stellar sidereal drift. The effect is discernable as a longitudinal variation in focus of the stellar trail because the CCD and corrector are not oriented orthogonally to the axis of the primary mirror. The surface of the CCD is thus tilted with respect to the focal plane and the trailed image, which maps the focal plane, reveals the focal variation. This method can detect the 575 arcsecond gross tilt error in this case, but is insensitive to tilt errors smaller than approximately 200 arcseconds. The determination of North-South tilt errors by comparing the defocusing of stars or stellar trails on opposite field edges is even less sensitive. For this reason the new PF assembly, to be installed in the fall of 2000, will have its level mechanically fixed by using the electronic level as a comparator with an absolute level reference (such as the leveled mirror). The level should not vary by more than a few tens of arcseconds due to thermal flexure, thus provision for tilt adjustment is not required.

Prime Focus Lateral Misalignment Image Suite I

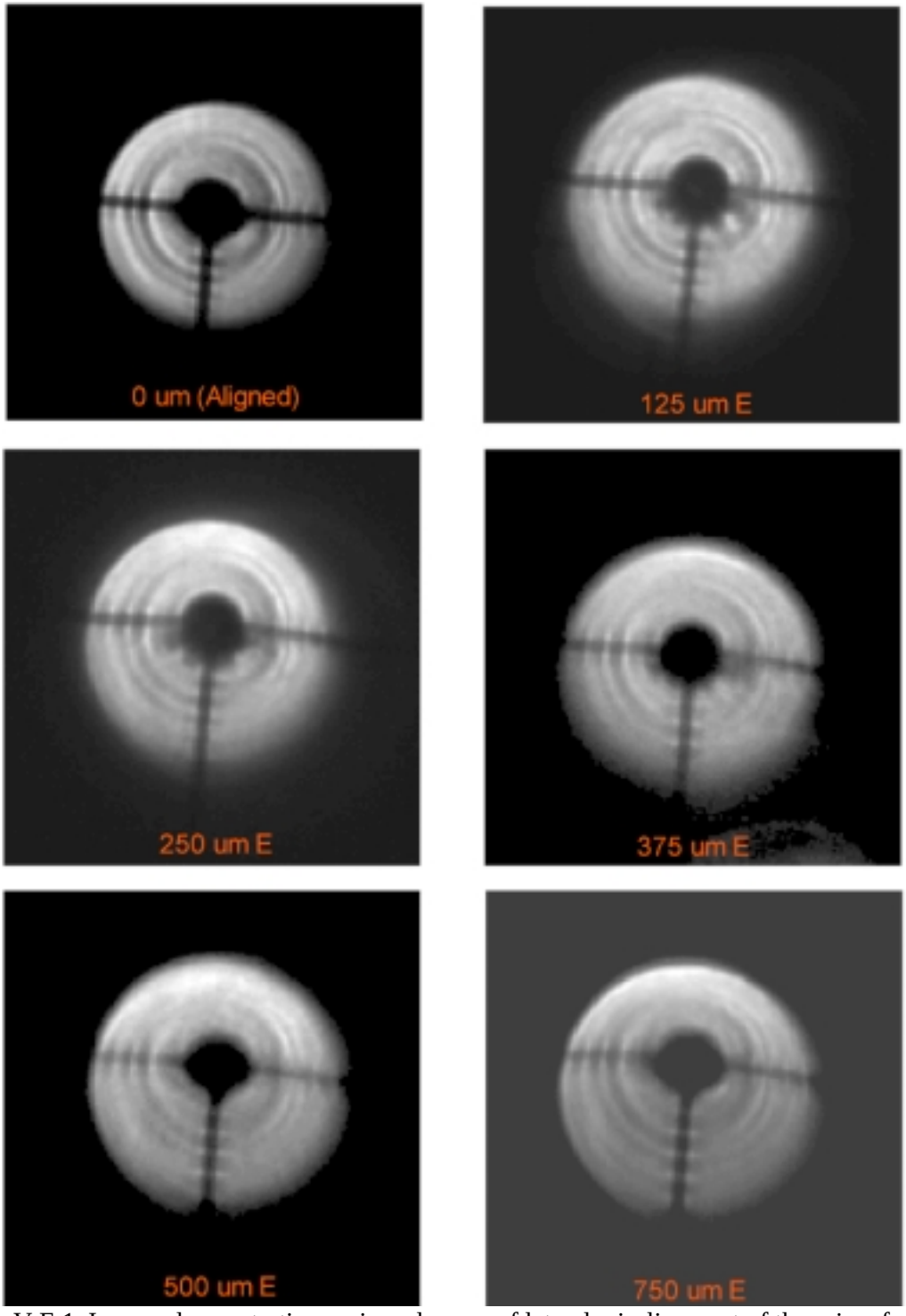

Figure V.F-1. Images demonstrating various degrees of lateral misalignment of the prime focus array. All images acquired 1600 um inside focus. (Images to scale)

Prime Focus Lateral Misalignment Image Suite II

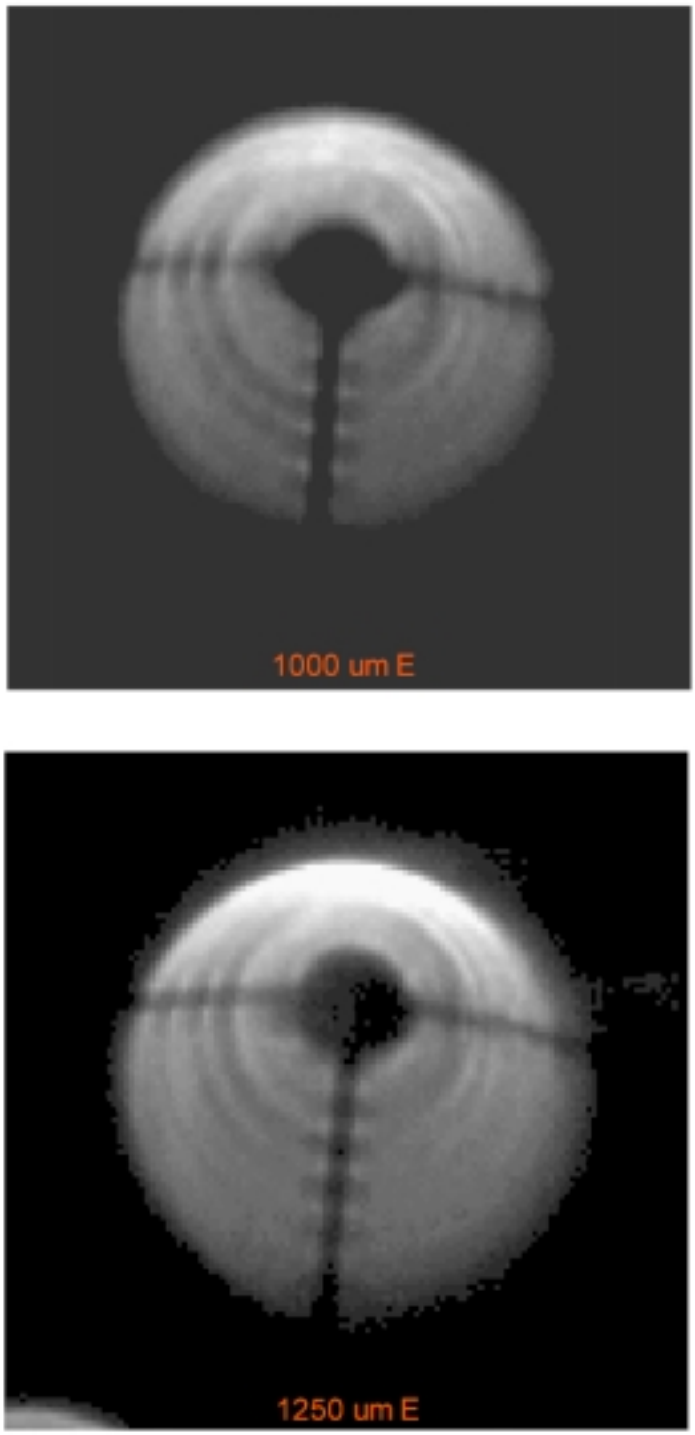

Figure V.F-2. Images demonstrating extreme lateral misalignment of the prime focus array. Both images acquired 1600 um inside focus. (Images to scale)

Focus Suite with 1250 um Lateral Prime Focus Misalignment

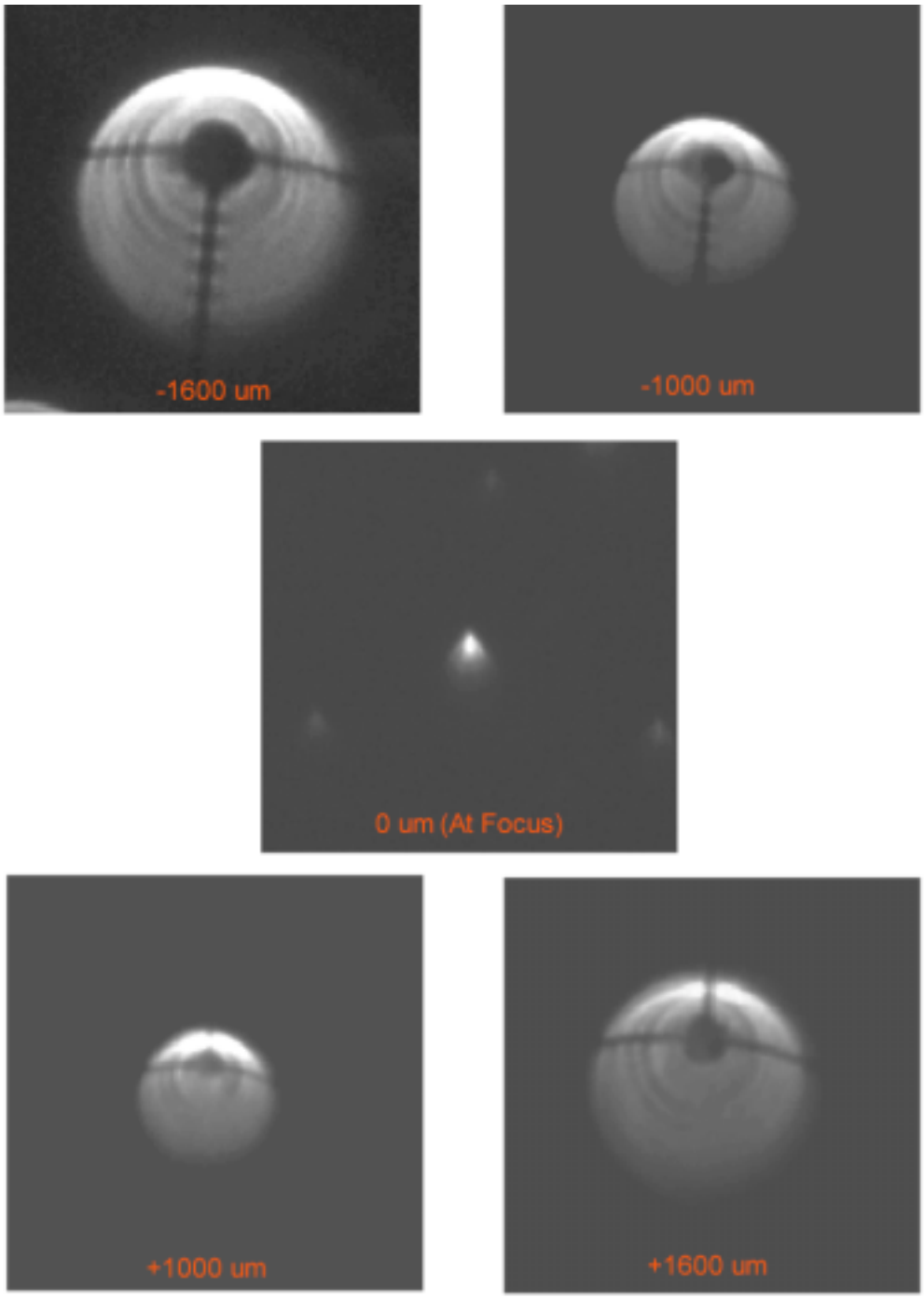

Figure V.F-3. Multiple Focal Position Suite demonstrating image quality as a function of focal position for a fixed 1250 um lateral misalignment of the prime focus array. Sequence moves from inside focus to the focal plane to outside focus. Note the significant flare at focus. (Images to scale)

Focus Suite with Prime Focus Laterally Aligned

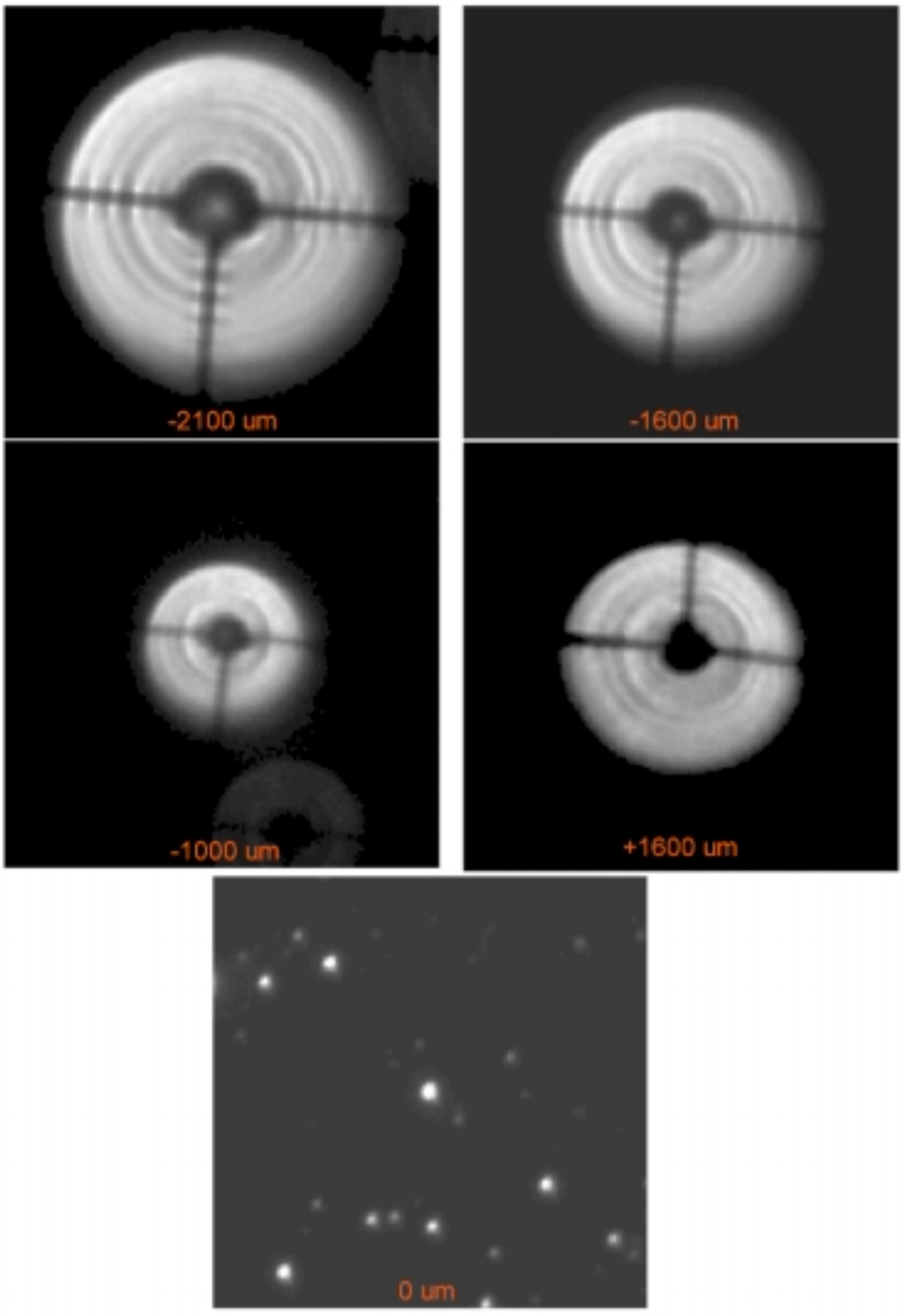

Figure V.F-4. Focal sequence demonstrating proper alignment of the LMT Prime Focus array and the resulting star images. Out-of-focus star images reveal the entrance pupil which in this sequence is almost symmetrical. The PF array (shadow) is well centered. The sequence moves from significantly inside focus to the focal plane where the star images are uniform. The outside focus image reveals a slight asymmetry possibly indicating a small tilt error.

Effect of Prime Focus Assembly Tilt on a Trailed Stellar Image

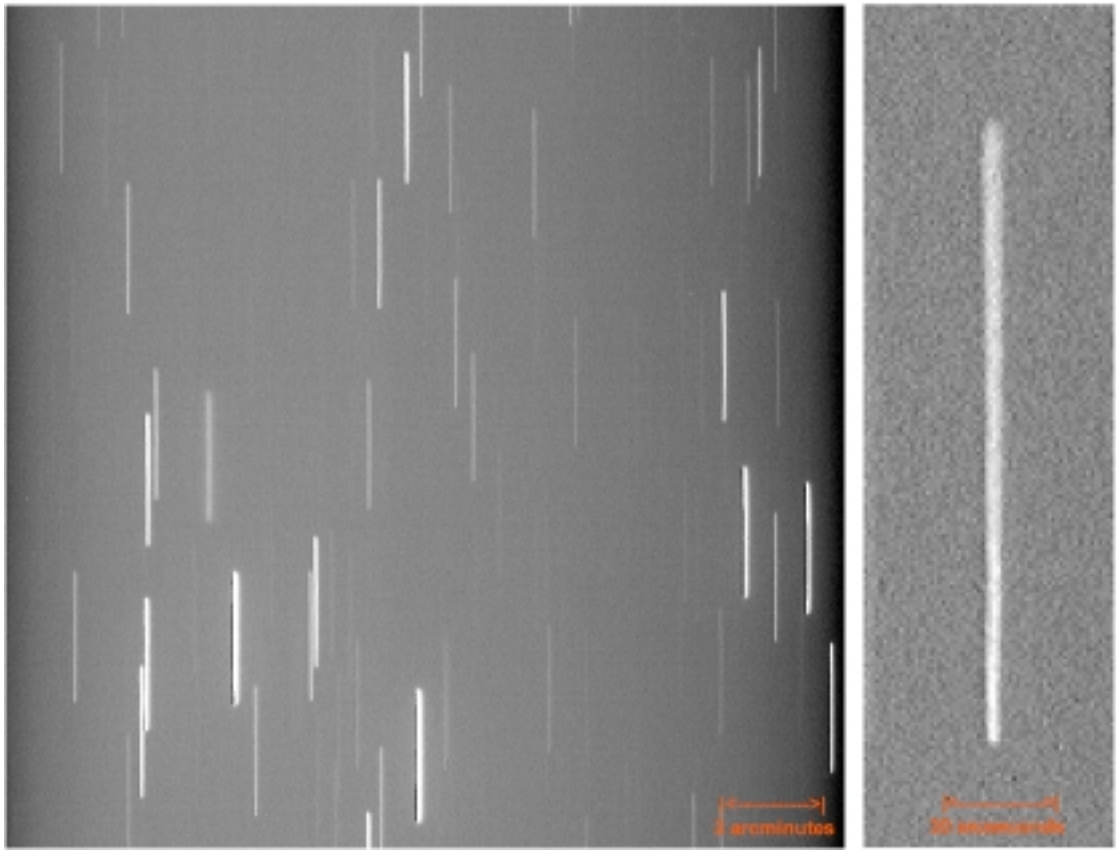

Figure V.F-5. A demonstration of the effect of Prime Focus tilt using a R Band trailed drift scan image of a random star field. The image was acquired with the PV1K CCD with a 0.960 arcsecond/pix plate scale yielding a 16.38 arcminute FOV. In this example, the prime focus array has been tilted from the horizontal plane by 575 arcseconds in the E-W direction. This yields a 68.7 um focal shift between the East and West edge of the CCD. The effect is observed in trailed star images (right inset) as a variable focus along the stars trajectory with a maximum focal difference at each end (corresponding to the CCD EW edges). It is easy to discern the effect of gross tilt in this example, but for smaller tilt errors where the focal variation is comparable to the allowable focal tolerance, the tilt effect would be not be discernable. For the NASA-LMT, the focal tolerance is approximately 27 um as set by the typical site seeing limit of 0.8 arcseconds and an allowable 5% defocusing. Therefore tilt errors smaller than approximately 200 arcseconds are not discernable by this technique. A more accurate method of sensing prime focus level (such as an electronic level) must be employed to achieve precision leveling to a few arcseconds. A NS tilt error would appear as a focal variation laterally across the FOV with maximum focal difference at the north and south field edges. The identical limitations apply as in the EW case.

G. Mirror Substrate Print-Through

In the alignment images shown in the previous section, the appearance of alternating light and dark annuli was evident in both the inside and outside focus images. The radial location of the bands is identical both inside and outside of focus implying that they are intrinsic to the mirror rather than a diffraction effect (Smartt PC). The location of the dark bands corresponds very closely to the boundaries which were delimited on the surface of the NASA liquid mirror container during the spin-casting process. The boundaries marked six equal-area annuli into which the liquid polyurethane was poured during spin-casting. This was done to ensure a spun-cast layer of uniform thickness and to minimize the amount of polyurethane (and working time) to be poured by any one of the six individuals assigned to an annulus. The demarcation between annuli is faintly visible with the unaided eye on the mirror substrate indicating that the boundary between annuli is somewhat discontinuous as might be expected from separate pours. It is likely that these radial discontinuities are printing through to the upper Hg surface of the mirror.

Figure V.G-1 shows a stellar image acquired 2.1 mm outside focus along with a surface map of the image generated with IRAF Imexamine. The numerical markers (pink) indicate the 5 of 6 radial positions which were measured and then compared with the 6 locations of the spin-cast boundaries. The 5^{th} position is not visible possibly because the scale of the outside focus image is not sufficient to resolve it from the peak between positions 4 and 6. Table V.G-1 compares the measured positions with the spin-cast boundary locations as a percentage of the mirror radius. The correlation is good, with

Possible Print-Through of the Mirror Substrate Spin-cast Annuli

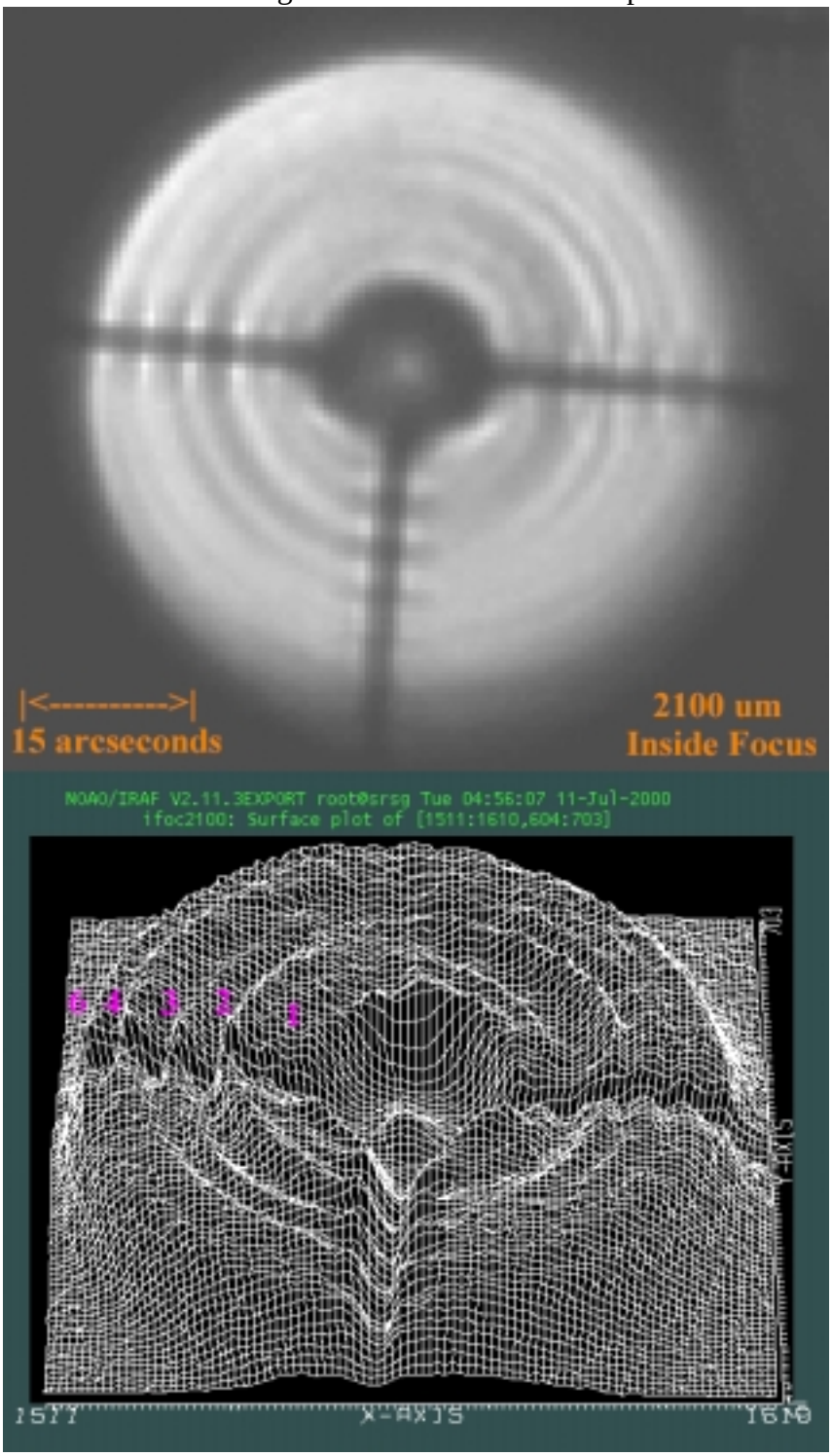

Figure V.G-1. A surface map of a stellar image acquired 2.1 mm inside focus. The dark bands (valleys) closely correspond to the boundaries between the 6 equal area annuli delimited on the mirror for spin-casting. It is possible that the large scale spin-cast defects are printing through to the Hg upper-surface.

position 4 in least agreement possible because of insufficient scale.

This defect illustrates the difficulty of accurately spin-casting the surface of a liquid mirror. Despite extensive practice by the individuals involved at NASA-JSC, large global defects were introduced into the spun-cast layer. These problems may be mitigated in future applications of the spin-cast process by using fewer annuli and taking additional care to ensure continuity at the boundaries. The Hickson LZT space frame and membrane design (Section IV.F) should obviate these problems.

The image degradation associated with the radial pattern is possibly manifest as a faint exponential halo observed surrounding the nominal Gaussian image cores in the NASA-LMT data. Hickson (PC) estimates that this scattered light halo contains as much as 10% of the object flux. A re-spincast of the NASA liquid mirror is being considered to rectify the print–through problem.

Table V.G-1 Comparison of Entrance Pupil Radial Pattern and Spin-cast Boundaries

	Mirror Numerical Position and as a % of Radius					
	1	2	3	4	5	6
Spin-cast Location	40.8 %	57.7	70.7	81.6	91.3	100
Entrance Pupil Location	41.3	58.7	71.7	85.8	NA	100

H. Atmospheric Seeing

Despite the scattered-light performance degradation possibly associated with spin-

cast print-through, the NASA-LMT has evolved to a state enabling optical resolution within the limitations set by the atmospheric seeing at NODO. Resolution matching the nominal seeing limit for NODO of 0.8 arcsecond (Smith and Salisbury 1961) has been attained by the NASA-LMT on the rare occasions (~5 nights/year) that this occurs. This is not to say that additional improvements cannot be made to the system, especially in terms of thinner Hg layers to facilitate wave damping, or the use of rotating or fixed baffling to reduce the intrinsic spiral waves and to improve angular velocity stability on windy nights. Additionally, the prime focus array as presently designed is prone to misalignment during camera and filter changes which are presently performed manually. The new PF assembly is automated and will eliminate this problem. If the NASA-LMT were moved to a site with better intrinsic atmospheric seeing, these improvement, along with a re-spincast, would probably be essential to regain seeing limited performance.

The performance limiting role of atmospheric seeing when the LMT system is otherwise performing optimally is illustrated in Figures V.H-1 through 3. These images demonstrate the obvious importance of conducting observations under optimal seeing conditions. Good seeing is important as well for differentiating between problems intrinsic to the telescope and otherwise. The mirror tilt experiments described in Section V.D were likely inconclusive because they were conducted with poor seeing.

To make optimum use of clear nights, orbital object observations with the MCP intensified video camera (2 arcseconds/pixel) are routinely performed in 2-4 arcsecond FWHM seeing conditions which are otherwise unacceptable for higher resolution astronomical or near-earth object (NEO) CCD data acquisition. The dual role of the

Spiral Galaxy NGC 3430 Seeing Comparison

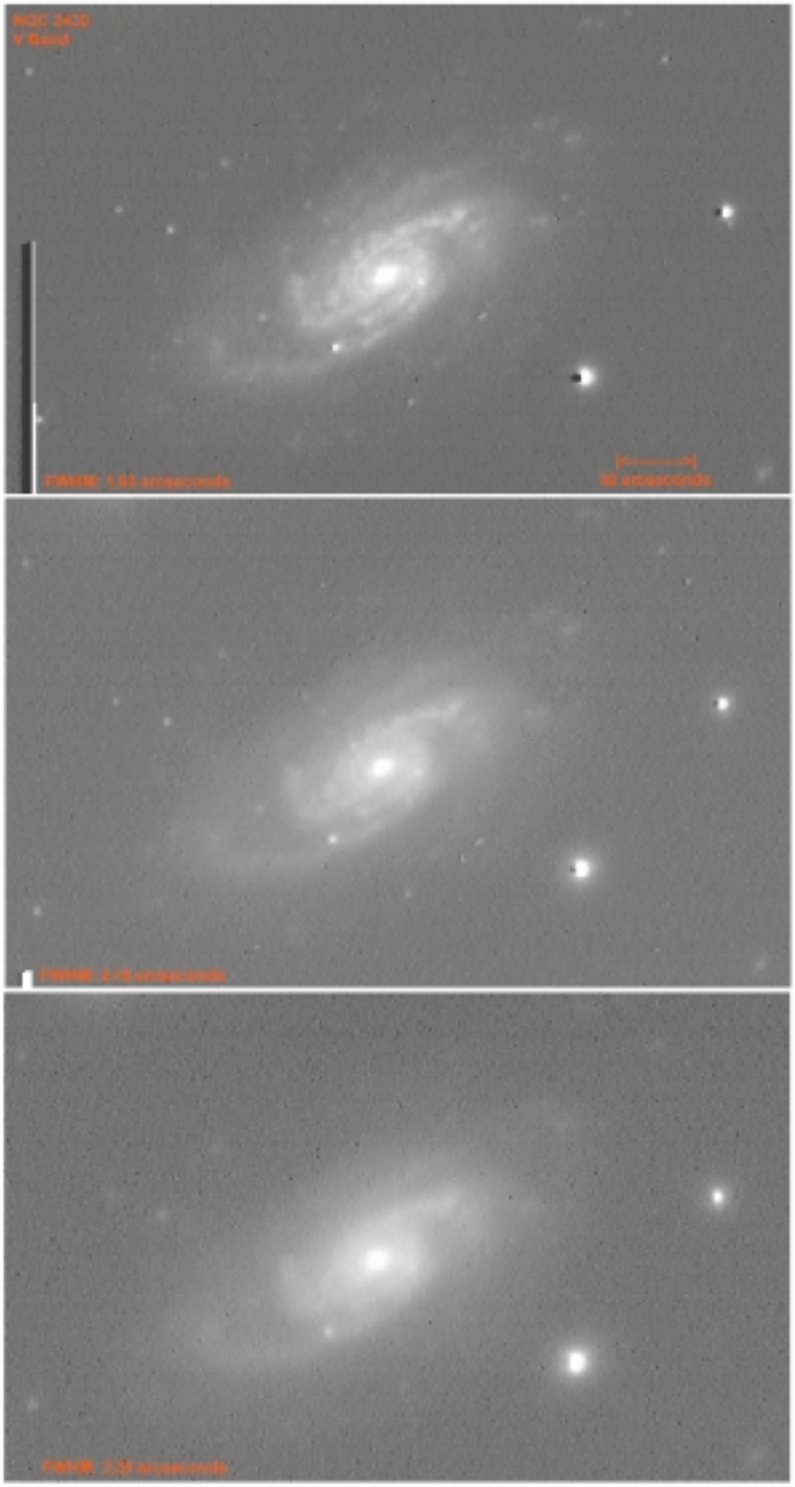

Figure V.H-1. V Band imagery of the 11.5 magnitude spiral galaxy NGC 3430 in Leo Minor under different seeing conditions. From top to bottom the mean measured FWHM of field stars is 1.63, 2.16, and 3.36 respectively. These images were acquired with the PV1K CCD (0.960 arcsecond/pixel) in the spring 1999 and 2000 observing seasons.

Planetary Nebula M57 Seeing Comparison

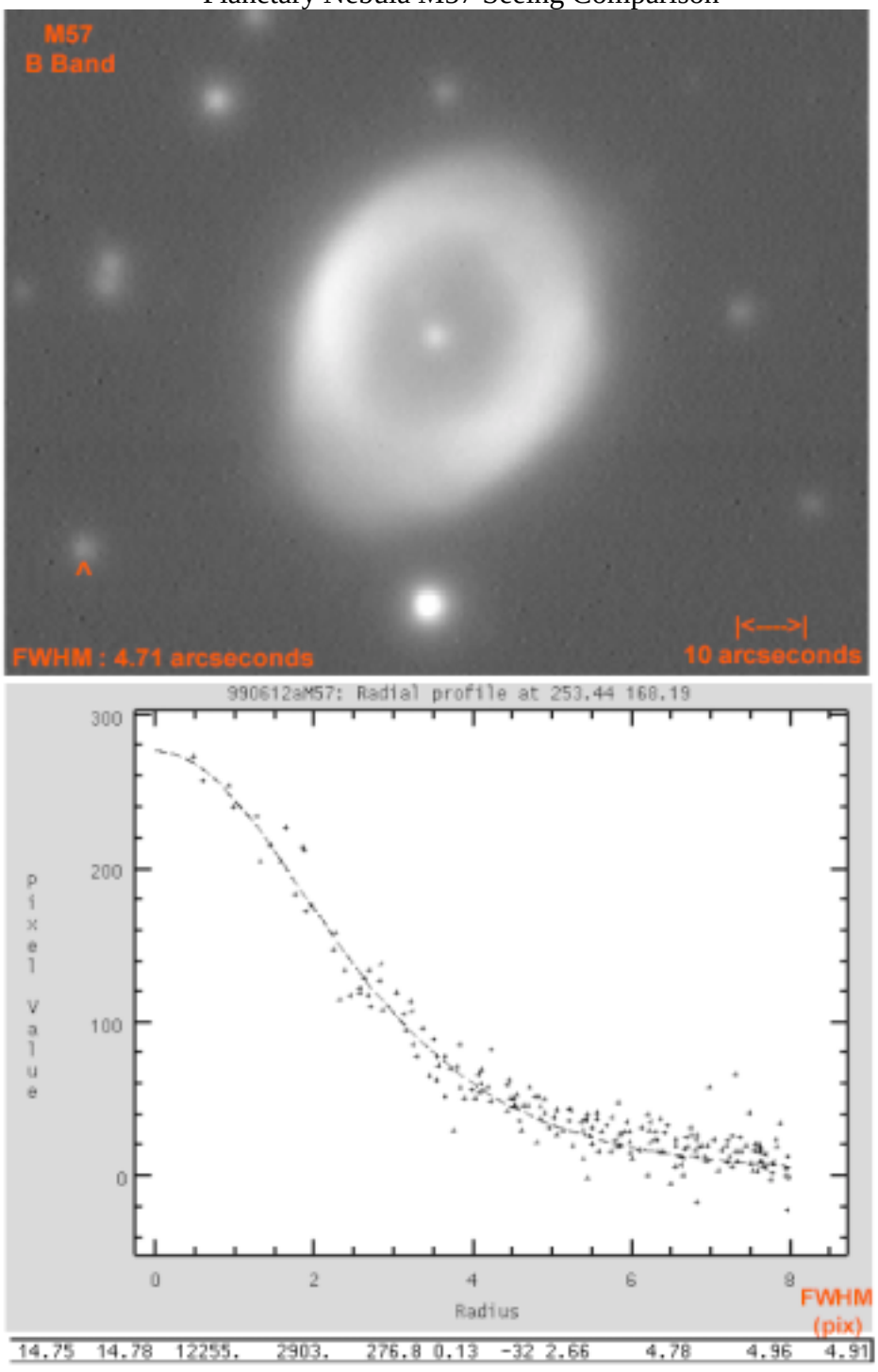

Figure V.H-2. B Band image of M57 acquired with the NASA-LMT using the PV 1K CCD. The image resolution is 4.71 arcseconds FWHM as measured from the intensity profile of a field star (red arrow). IRAF Imexamine was used to generate the radial profile and the Gaussian fit. The lower numerical string contains measured photometric and astrometric parameters for the star, terminating with the FWHM in pixels. Compare this image with the following figure.

Planetary Nebula M57 Seeing Comparison

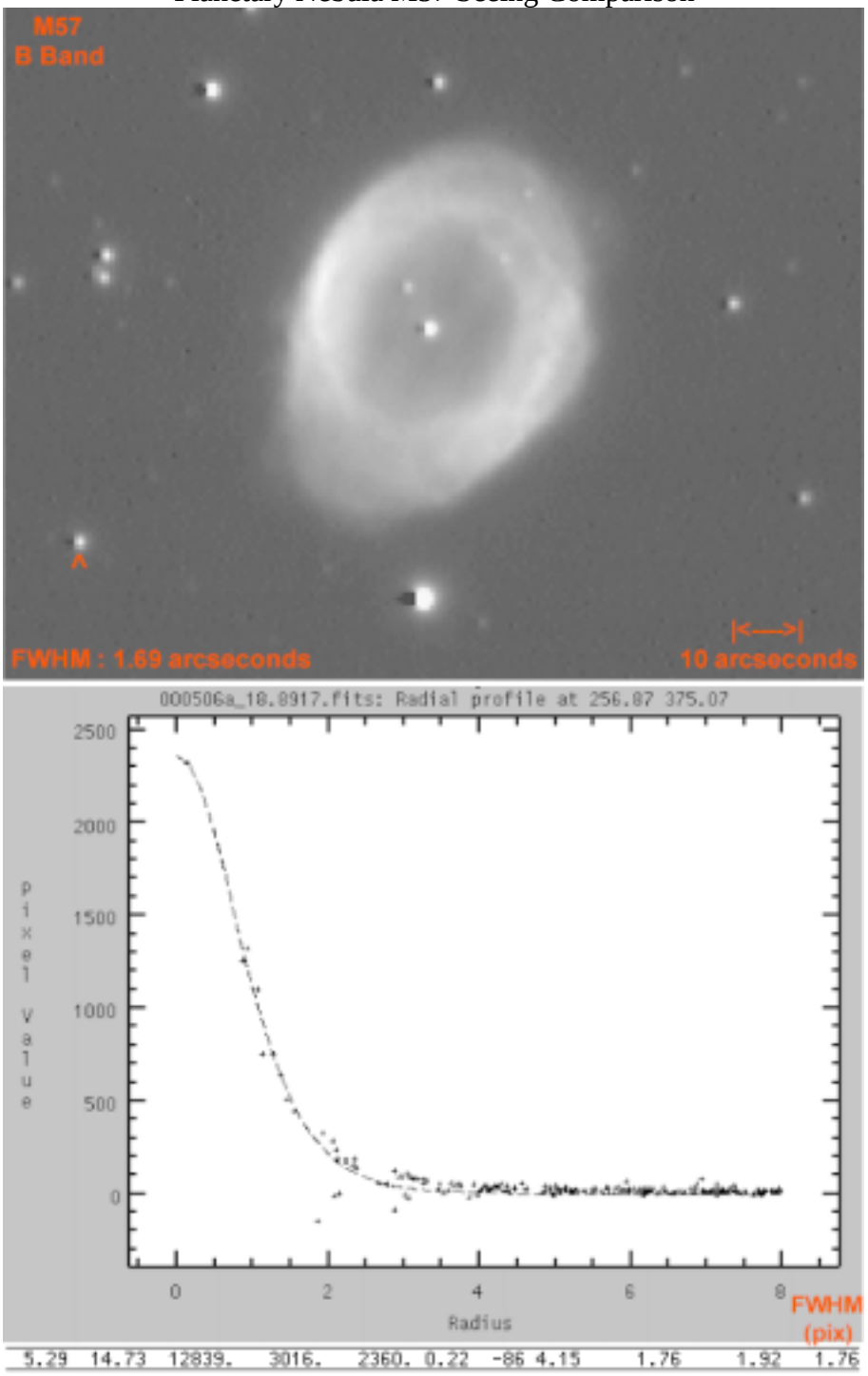

Figure V.H-3. B Band image of M57 acquired with the NASA-LMT using the PV 1K CCD. The image resolution is 1.69 arcseconds FWHM as measured from the intensity profile of a field star (red arrow). IRAF Imexamine was used to generate the radial profile and the Gaussian fit. The lower numerical string contains measured photometric and astrometric parameters for the star, terminating with the FWHM in pixels. Compare this image with the previous figure.

NASA-LMT can thus frequently be fulfilled with minimal conflict, especially so when coupled with the normally twilight conditions under which orbital object observations are made.

The role of local dome seeing has not been fully characterized with respect to image performance at NODO. Dome exhaust fans are used occasionally to help equilibrate the dome and external environment, but no clear pattern has emerged as to the efficacy of this procedure. The installation of a pier cooling system is planned for the summer of 2001 to evaluate the benefits of maintaining the mirror surroundings $\sim 2\,^{0}C$ cooler than the environment to minimize upwardly directed convective turbulence (as has been employed to positive effect at other observatories).

I. Moisture Condensation

In addition to atmospheric seeing, local environmental conditions affect the NASA-LMT image quality. The role of external wind in terms of mirror speed stability and the introduction of vibrations which can cause concentric waves has been discussed in Chapter III. A high dust count can reduce mirror reflectivity, scatter incoming light, or brighten the ambient background.

Operation of the LMT in conditions near the local dew-point can be detrimental to performance as well. In addition to the possibility of condensation on the primary mirror, other optical surfaces including the CCD camera window can be affected. CCD camera heads are evacuated to prevent convective cooling of the dewar window by the

cooled CCD. There is some radiative cooling of the window however as well as cooling of the entire camera head if a refrigerated liquid jacket is used to extract heat from a thermoelectrically cooled CCD. Prior to the use of a clean dry air jet across the CCD window, dewing presented an intermittent problem at NODO and an almost continuous problem at NASA-JSC. Figures V.I-1 and 2 demonstrate the effect of camera dewing on image quality. The NASA-JSC example is an extreme case where the entire CCD window had accumulated moisture. The NODO example is more typical, with the formation of a dew spot at the window's center.

J. Miscellaneous Optical Phenomena

A variety of phenomena arising from the unique nature of the LMT have been observed in the imagery data acquired with the NASA-LMT. Three of the examples presented here demonstrate optical effects specific to the rotating liquid mirror. The fourth example could occur in any telescopic system using a CCD. The phenomena include the appearance of circular rings, both concentric and offset with respect to stars, which may be related to concentric waves on the mirror surface, radially oriented spokes seen rotating at the mirror angular velocity in MCP intensified video data presumably due to waves and print through defects, and a square diffraction pattern visible around very bright stars arising from the CCD behaving as a grating.

The first example of the circular ring pattern is shown in Figure V.J-1. Acquired through a 10 nm wide interference filter centered at 688 nm, the observed rings vary in

Image Degradation Due to Condensation on the CCD Camera Head Optical Window

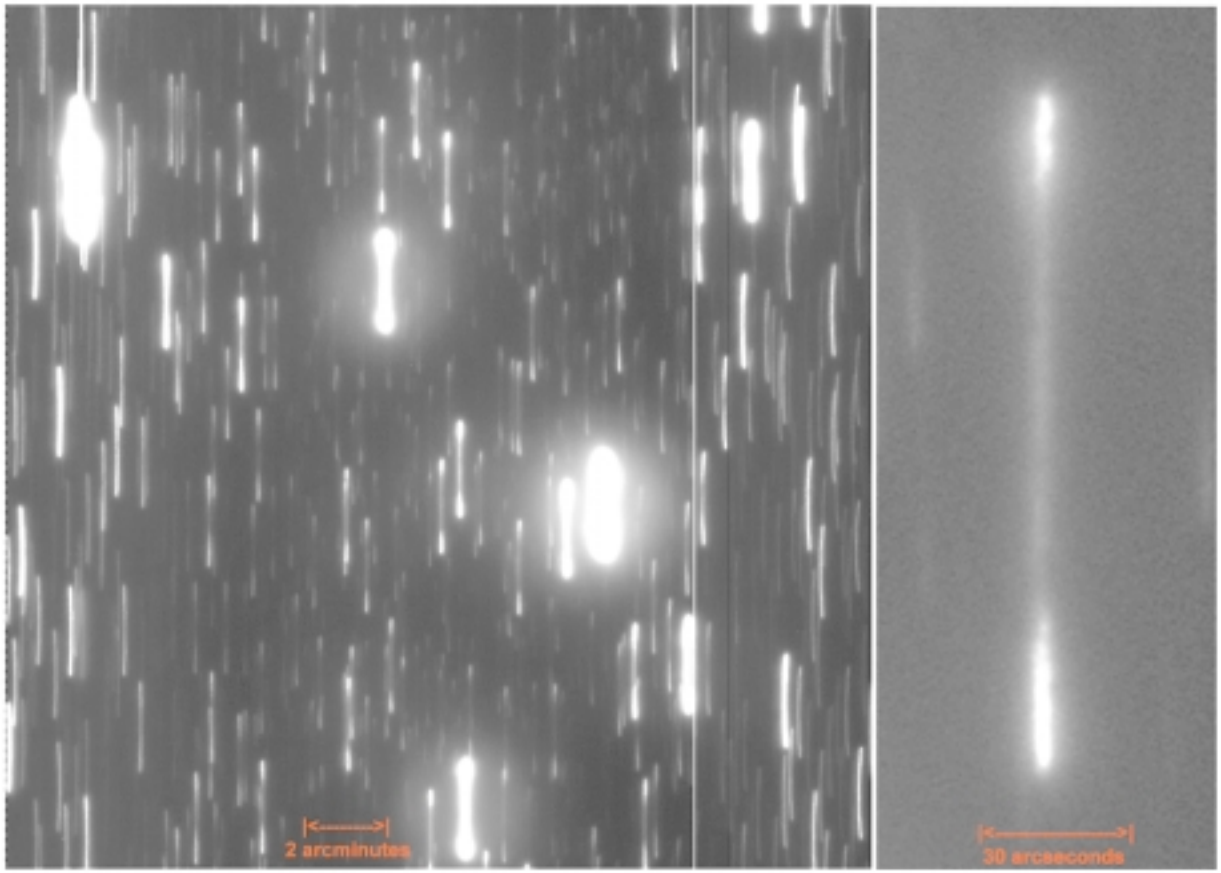

Figure V.I-1. A demonstration of the effect on image quality of moisture condensation on the CCD Camera Head optical window. Radiative cooling of the window by the CCD can cause the formation of condensate on the window during conditions of high relative humidity. The spot forms in the window center and spreads radially outward if dewing conditions persist. In this example, the star trails are obscured by a dew spot formed in the window center while the window perimeter remains clear. The introduction of a clean dry air stream (–30 C dew point) across the CCD window has eliminated this problem. The air is channeled from the air bearing supply. Image was acquired with the LSP 2K CCD.

Image Degradation Due to Condensation on the CCD Camera Head Optical Window

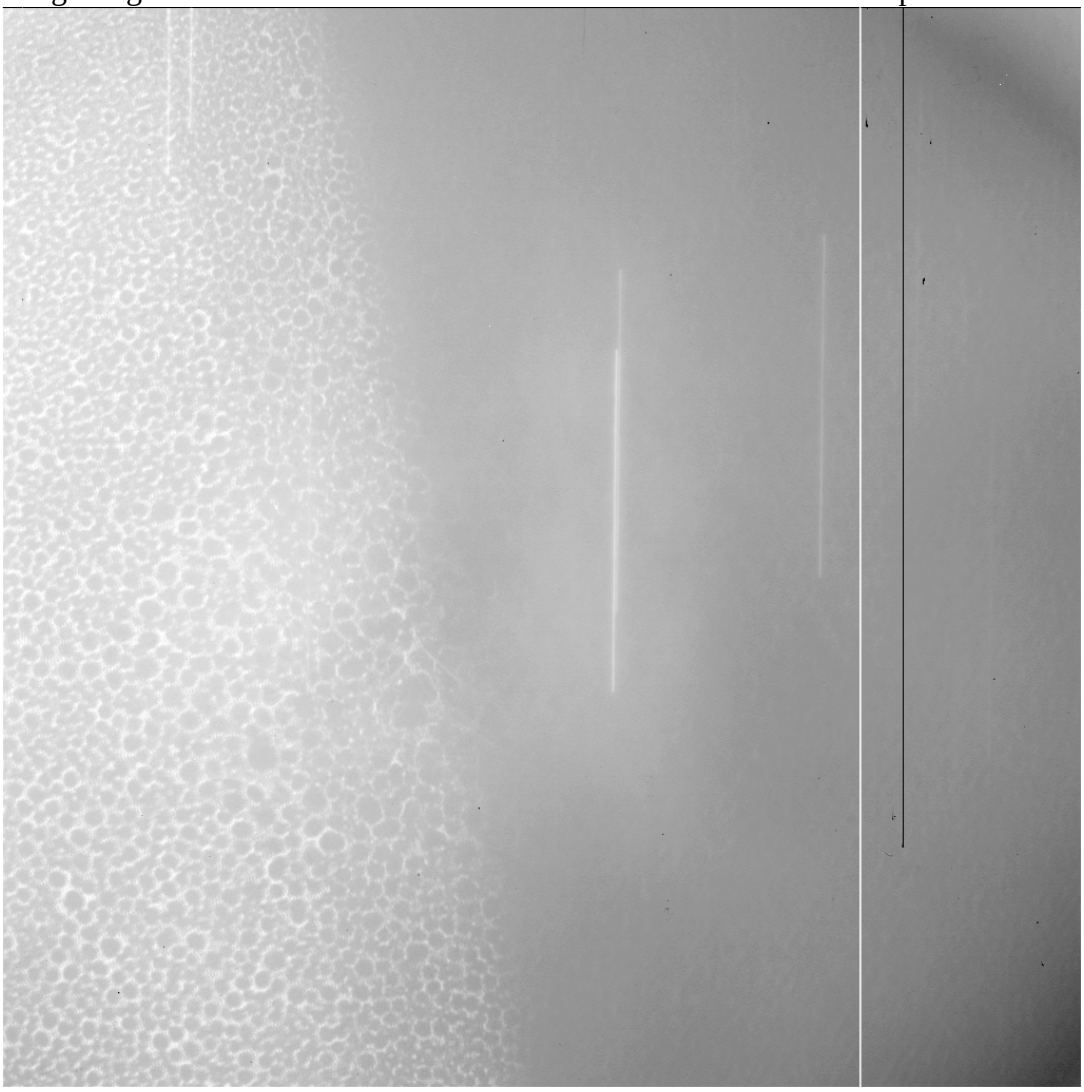

Figure V.I-2. A demonstration of the effect on image quality of moisture condensation on the CCD Camera Head optical window. Radiative cooling of the window by the CCD can cause the formation of condensate on the window during conditions of high relative humidity. The refrigerated circulating fluid which cools the Petier Thermoelectric device via a water-jacket can also cool the entire camera head below the dew point. This can result in the formation of a tremendous amount of condensation as in this example. The shadow of the water droplets are clearly visible on the left side of the field on this moonlit night at NASA-JSC. Only rarely does dewing this severe occur at NODO. As with the condensation induced from radiative cooling, the introduction of a clean dry air stream (–30 C dew point) across the CCD window helps mitigate this problem as long as moisture does not migrate into the field from the body of the camera head. Image was acquired with the LSP 2K CCD.

Circular Stellar Diffraction Pattern

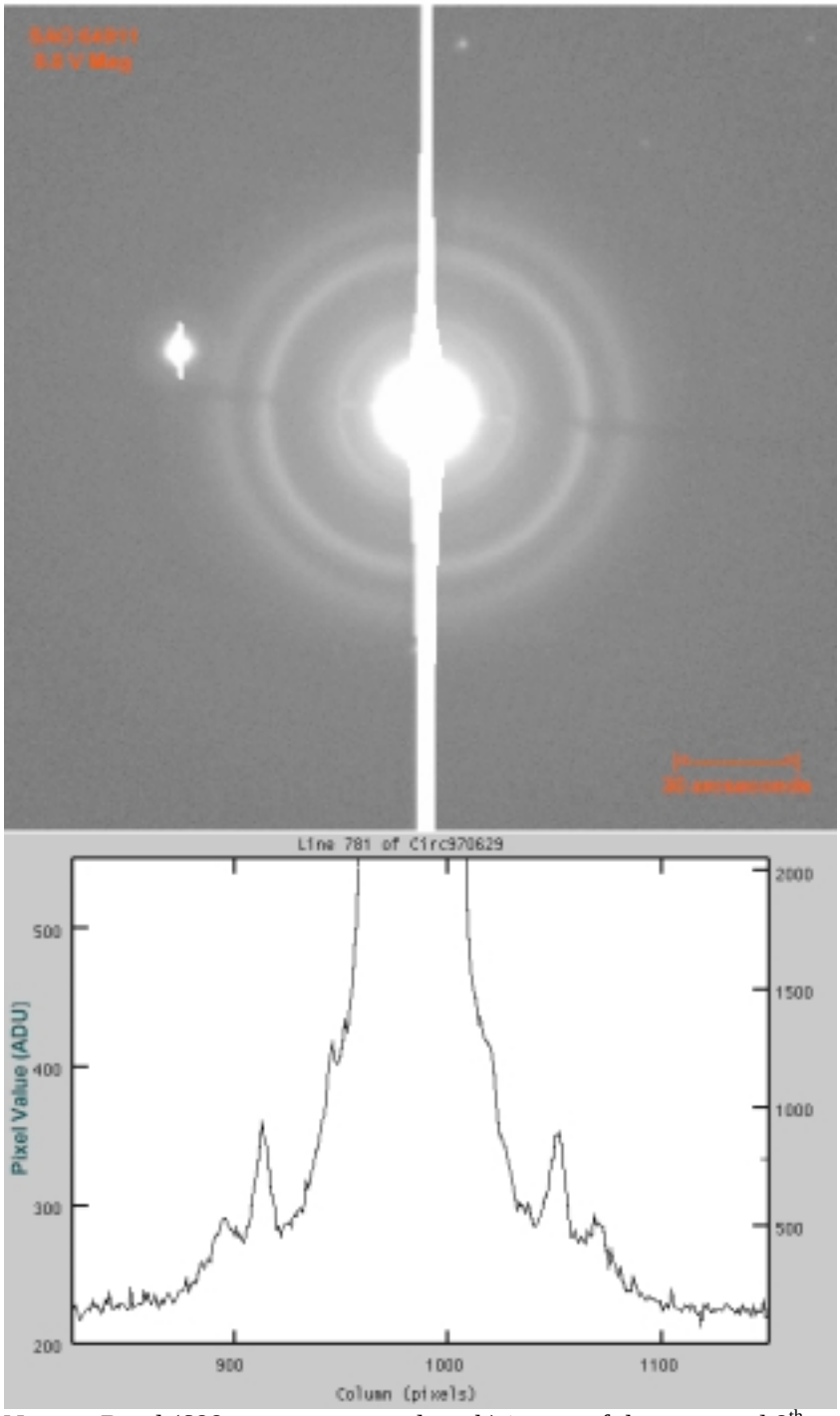

Figure V.J-1. Narrow Band (688 nm center wavelength) image of the saturated 8th magnitude (V) star SAO64911 in Corona Borealis.The rarely observed circular diffraction pattern is as yet unexplained, but is possibly due to concentric waves on the mirror surface. The row cross-sectional plot (generated with IRAF implot) is shown to facilitate further investigation. The image was acquired with the LSP 2K CCD with a 0.598 arcsecond/pix plate scale. The brightest ring is ~78 arcseconds in diameter.

diameter from approximately 45 to 96 arcseconds. Since careful adjustment and testing has verified that they are not the result of internal reflections, it is possible they are diffraction products arising from the concentric waves on the mirror surface. From the relation $n \cdot \lambda = D \cdot \sin\Theta$ (exact for plane parallel diffraction, but approximate for the circular case which involves Hankel transforms; Hickson PC), the ratio of the concentric wavelength (D in mm) and the order (n), that yields constructive interference from the concentric waves on the liquid mirror, varies from D/n = 2.46 to 3.15 mm for the angular diameter range of circular rings observed. From Chapter III, the range of observed concentric wavelengths on the liquid mirror surface is approximately 6.8 mm to 17 mm. Thus orders from n = 2 to 7, depending upon the concentric wavelength, will satisfy the (D/n) relationship and produce the observed rings. For any observed concentric wavelength on the mirror surface, the order n = 1 is not represented because the angular extent of the circular ring would place it too close to the central star to be visible. The same is true for orders less than n = 5 for the 17 mm concentric waves. Although these discreet concentric rings are not visible in the broadband filtered imagery because of the absence of monochromaticity, they are nonetheless present as a continuum and therefore contribute to the scattered light around the Gaussian PSF.

Figure V.J-2 shows a group of single circular rings offset from their associated stars. This R-Band filtered image is not approximately monochromatic as in the previous example and is thus difficult to associate with the diffraction effect from concentric waves. The rings are approximately 26.4 arcseconds in diameter. Repeated attempts were made to correlate their appearance with internal reflections by repositioning the filter and

Diamond Ring Reflection and Tilted LM Cardioids

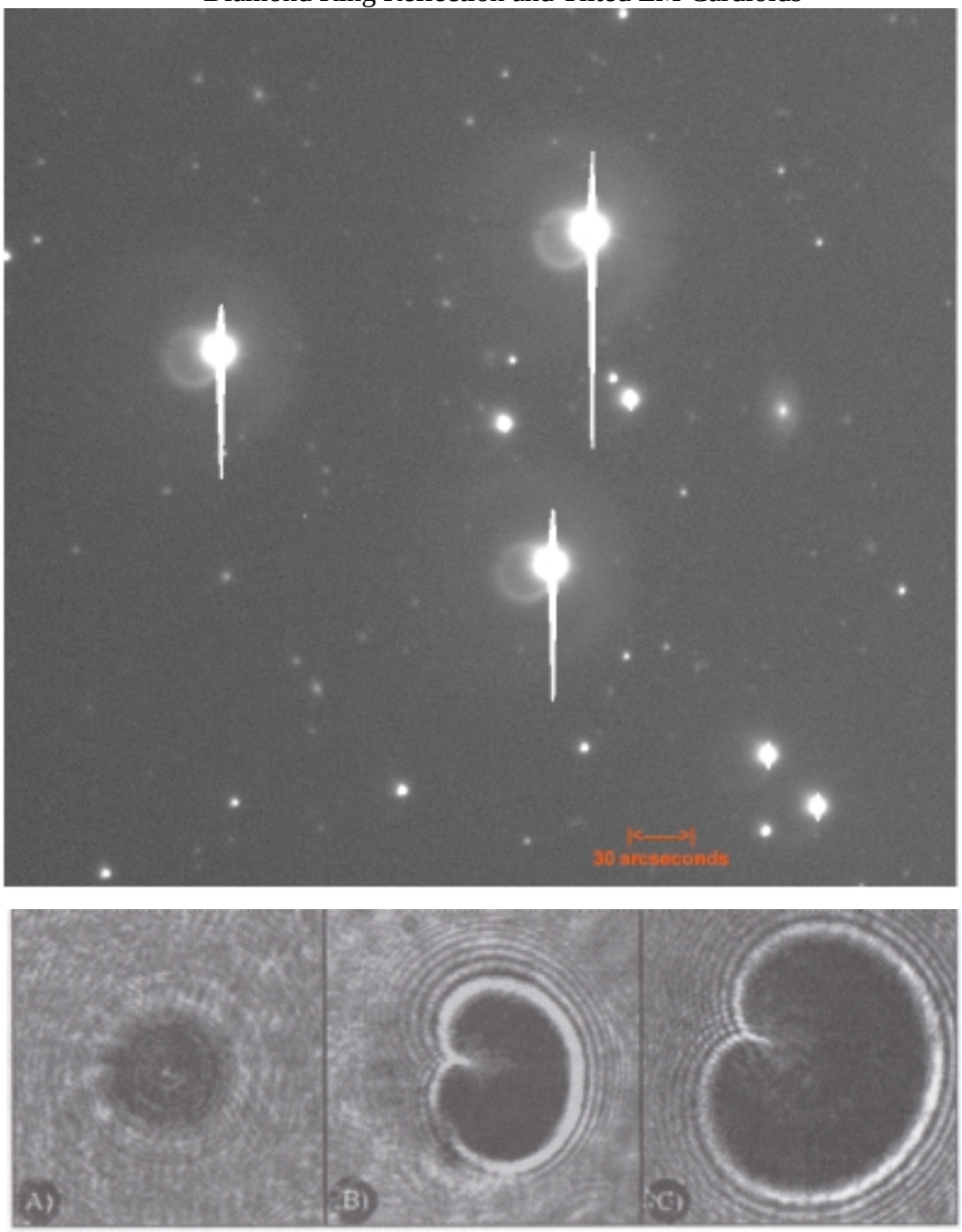

Figure V.J-2. Upper: R Band image of a 10 to 12 magnitude (V) stellar quartet in Canes Venatici. The peculiar diamond ring reflection is attributable to imperfect leveling of the LMT primary mirror. The physical mechanism yielding this aberration is not yet understood. The reflection is not due to any misalignment associated with the prime focus array nor is it due to internal reflections in the filter used. Lower: Entrance pupil cardioids observed by Girard and Borra (1997) near the center of a 2.5 m LM de-leveled by 0, 1 and 3 arcseconds respectively. These cardioids can be used to accurately level a LMT and may be related to the offset rings.

CCD camera and altering the prime focus alignment, but to no avail. The rings were eventually eliminated when the primary mirror rotational axis was re-leveled from a misalignment of approximately 2.5 arcseconds. The reason for this is unclear and perhaps coincidental, although Girad and Borra (1997) have observed a cardioid shaped defect in the out of focus entrance pupil images of liquid mirrors with 1 and 3 arcsecond leveling errors. The defect appears near the center and edges of the liquid mirror and can be used to accurately level the rotational axis. Further investigation will determine if this asymmetrical defect causes the offset ring.

Figure V.J-3 shows two video frames separated by 1/10th of a second illustrating the rotation of radial spokes visible in the halo around bright stars. The spokes rotate at the same angular velocity as the mirror and are presumably associated with local defects on the Hg surface. Supporting evidence for surface defects as the source comes from the observation that the number and radial extent of the spokes correlates positively with windy conditions.

Figure V.J-4 shows the presumably ubiquitous square diffraction pattern observed in the vicinity of bright stars. The closely spaced (24 um) CCD rows and columns act as a diffraction grating for all sources, but the pattern is only visible if the source star is extremely bright (3.7 V magnitude in this case).

Rotating Radial Spoke Pattern

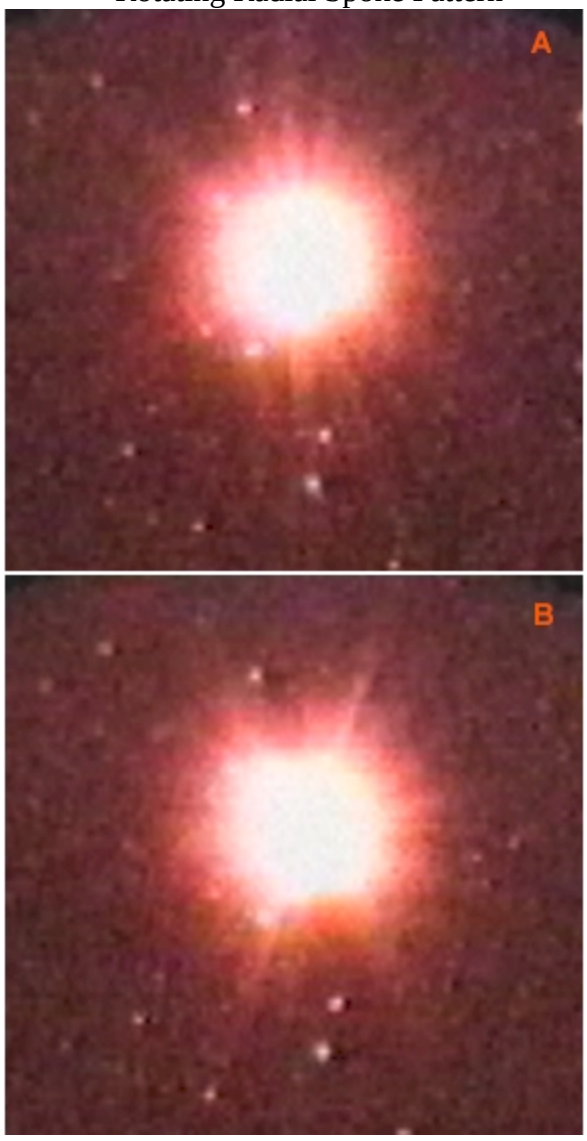

Figure V.J-3. A pattern of rotating radial spokes in a focused image of a bright (~4th magnitude) star. The spokes, which rotate at the same angular velocity as the mirror, only appear during windy conditions. They are presumed related to surface defects on the mirror substrate or to waves on the mirror surface. These video frames separated by 1/10th second were acquired with the 40mm MCOP intensified video camera.

ν Ursa Majoris and CCD Diffraction Grating Effect

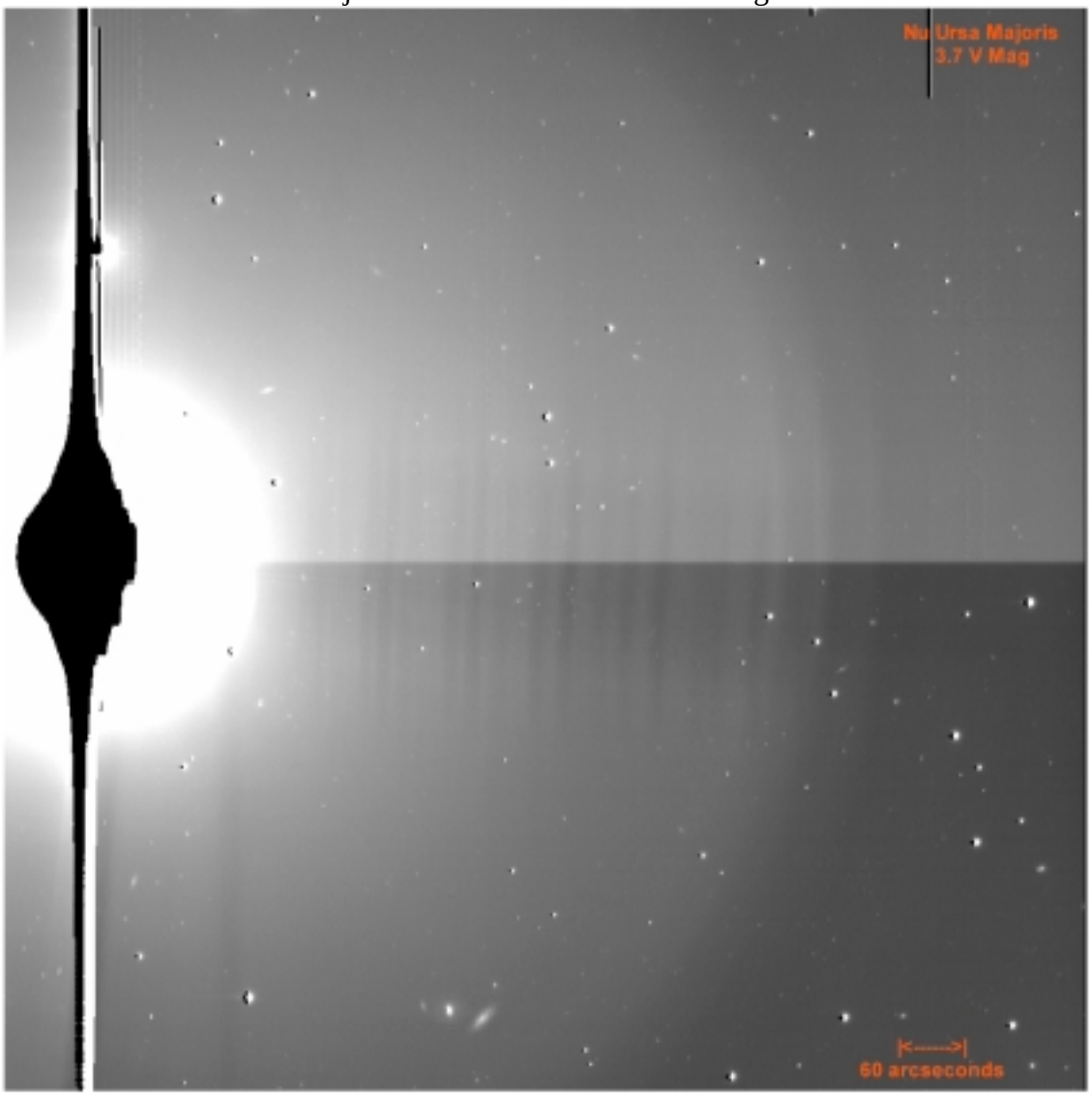

Figure V.J-4. R Band image of the 3.7 magnitude (V) star ν Ursa Majoris. The saturated star is sufficiently bright that a diffraction pattern resulting from the grating effect of the CCD rows and columns is visible extending across the field as alternating dark and light bands. The image was acquired with the PV 1K CCD with a 0.960 arcsecond/pix plate scale.